

# **CFD SIMULATION OF A TRIPROPELLANT ROCKET ENGINE COMBUSTION CHAMBER**

a project presented to

The Faculty of the Department of Aerospace Engineering San José State University

in partial fulfillment of the requirements for the degree

*Master of Science in Aerospace Engineering*

by

**Mani Subramanian**

August 2019

approved by

Dr. Periklis Papadopoulos

Faculty Advisor



## Abstract

Since the inception of rocket-powered flight the vast majority of rocket engine designs have involved the use of one fuel and one oxidizer. The fuel in modern designs have most commonly been either high-density liquid kerosene or low-density liquid hydrogen, while the oxidizer has most commonly been liquid oxygen. The exclusive use of one fuel over another places limits on the operational efficiency of a rocket system at different flight regimes. A tripropellant engine, one which burns two different fuels with the same engine, overcomes these limits.

Conceptual studies of tripropellant rocket engines have been previously done and experimental tripropellant engines have been built before, but their developments have been stalled due to the high cost of research and prototype testing. This study seeks to leverage the use of CFD to cheaply investigate the tripropellant engine concept. Initially, research was done into prior investigations of the tripropellant concept as well as into general CFD simulation of rocket combustion chambers. From this research, a benchmark 2-D unsteady CFD simulation case was replicated and used as a stepping stone to investigate the effects of different mixture rates on a tripropellant rocket combustion chamber burning liquid hydrogen, liquid kerosene, and liquid oxygen.

Four major scenarios of combustion were investigated: equal flow rates of hydrogen and kerosene into the combustion chamber, higher hydrogen flow rates, higher kerosene flow rates, and higher oxygen flow rates. The pressure and temperature results of these four scenarios are presented and an analysis of the results and comparison to each other was done.

## Contents

1.	Chapter 1 - Introduction.....	1
1.1	Motivation.....	1
1.1	Project Proposal.....	2
2.	Chapter 2 - Literature Review.....	3
2.1	Basic Rocket Engine Theory.....	3
2.2	Summary of Previous Research into the Tripropellant Concept.....	3
2.2.1	Tripropellant Rocket Technology for Reusable Launch Vehicles.....	3
2.2.2	Russian Tripropellant Engines for SSTO.....	5
2.2.3	Development of Tripropellant CFD Design Code.....	5
2.2.4	Tripropellant Combustion Process.....	6
2.3	CFD Simulation of a Liquid Rocket Propellant (LH2/Lox) Combustion Chambers.....	6
2.3.1	CFD Simulation of a Liquid Rocket Propellant (LH2/Lox) Combustion Chambers.....	6
2.3.2	Numerical Modelling of Liquid Oxygen and Kerosene Combustion at High Pressures.....	7
2.3.3	CFD Spray Combustion Model for Liquid Rocket Engine Injector Analyses.....	8
2.3.4	Modelling of Combustion and Heat Transfer in Rocket Combustion Chambers Using CFX.....	8
2.3.5	Navier-Stokes Flowfield and Performance Analysis of Liquid Rocket Engines.....	9
2.3.6	Three-Dimensional Numerical Analysis of LOX/Kerosene Engine Exhaust Plume Flow Field Characteristics.....	9
2.3.7	Subscale Hydrogen/Oxygen Combustion Chamber Experiment.....	9
3.	Chapter 3 - Methodology.....	12
4.	Chapter 4 – Theory.....	13
4.1	Combustion and Reacting Flow.....	13
4.1.1	Chemical Kinetics.....	13
4.1.2	Equilibrium Chemistry.....	14
4.2	Isentropic Expansion.....	17
4.3	Boundary Layer Flow.....	18
5.	Chapter 5 – Governing Equations.....	21
6.	Chapter 6 – CFD Code Overview.....	23
6.1	Solver Settings.....	23
6.1.1	Two Dimensional.....	24
6.1.2	Unsteady, Segregated Flow, and Segregated Enthalpy.....	24
6.1.3	Reacting Species Transport, Eddy Break-Up, Multi-Component Gas, Segregated Species.....	24
6.1.4	Reynolds-Averaged Navier-Stokes, Standard K-Epsilon, K-Epsilon Turbulence.....	25
7.	Chapter 7 – Validation Test Case.....	26
7.1	Testcase.....	26
7.1.1	Geometry.....	26
7.1.2	Mesh.....	26
7.1.3	Simulation.....	27
7.1.4	Results.....	28
8.	Chapter 8 – Tripropellant Simulation.....	30
10.1	Kerosene Injection Configuration.....	30

10.2	Kerosene and Oxygen Chemical Reaction .....	31
10.3	Scenario 1: Matching Hydrogen and Kerosene Mass Flow Rates .....	32
	10.3.1 Mole Concentration of Reactants and Products.....	32
	10.3.2 Temperature and Pressure Distribution .....	34
10.4	Scenario 2: Higher Kerosene Mass Flow Rate than Hydrogen.....	36
	10.4.1 Mole Concentration of Reactants and Products.....	36
	10.4.2 Temperature and Pressure Distribution .....	38
10.5	Scenario 3: Higher Hydrogen Mass Flow Rate than Kerosene.....	40
	10.5.1 Mole Concentration of Reactants and Products.....	40
	10.5.2 Temperature and Pressure Distribution .....	41
10.6	Scenario 4: Higher Oxygen Mass Flow Rate .....	43
	10.6.1 Mole Concentration of Reactants and Products.....	43
	10.6.2 Temperature and Pressure Distribution .....	45
10.7	Conclusion.....	47
9.	References.....	48

## Figures

Figure 1. Temperature distribution across combustion chamber and nozzle. ....	10
Figure 2. Graphical representation of temperature distribution across combustion chamber and nozzle. ....	11
Figure 3. Schematic of a supersonic nozzle. ....	18
Figure 4. Velocity gradient within the boundary layer. ....	20
Figure 5. Physics set up of the simulation. ....	23
Figure 6. 2D Geometry. ....	26
Figure 7. Generated mesh. ....	27
Figure 8. Mesh detail near the boundaries of the geometry. ....	27
Figure 9. Temperature variation from combustion chamber to nozzle exit. ....	28
Figure 10. Graphical representation of temperature variation from combustion chamber to nozzle exit. ....	29
Figure 11. Injector region. ....	31
Figure 12. Hydrogen concentration variation across the chamber and nozzle. ....	32
Figure 13. Oxygen concentration variation across the chamber and nozzle. ....	32
Figure 14. Kerosene concentration variation across the chamber and nozzle. ....	33
Figure 15. Water concentration variation across the chamber and nozzle. ....	33
Figure 16. Carbon-dioxide concentration variation across the chamber and nozzle. ....	33
Figure 17. Qualitative temperature distribution across the chamber and nozzle. ....	34
Figure 18. Quantitative temperature distribution across the chamber and nozzle. ....	34
Figure 19. Qualitative pressure distribution across the chamber and nozzle. ....	35
Figure 20. Quantitative pressure distribution across the chamber and nozzle. ....	35
Figure 21. Kerosene concentration variation across the chamber and nozzle. ....	36
Figure 22. Water concentration variation across the chamber and nozzle. ....	37
Figure 23. Carbon-dioxide concentration variation across the chamber and nozzle. ....	37
Figure 24. Qualitative temperature distribution across the chamber and nozzle. ....	38
Figure 25. Quantitative temperature distribution across the chamber and nozzle. ....	38
Figure 26. Qualitative pressure distribution across the chamber and nozzle. ....	39
Figure 27. Quantitative pressure distribution across the chamber and nozzle. ....	39
Figure 28. Hydrogen concentration variation across the chamber and nozzle. ....	40
Figure 29. Water concentration variation across the chamber and nozzle. ....	40
Figure 30. Carbon-dioxide concentration variation across the chamber and nozzle. ....	41
Figure 31. Qualitative temperature distribution across the chamber and nozzle. ....	42
Figure 32. Quantitative temperature distribution across the chamber and nozzle. ....	42
Figure 33. Qualitative pressure distribution across the chamber and nozzle. ....	43
Figure 34. Quantitative pressure distribution across the chamber and nozzle. ....	43
Figure 35. Oxygen concentration variation across the chamber and nozzle. ....	44
Figure 36. Water concentration variation across the chamber and nozzle. ....	44
Figure 37. Carbon-dioxide concentration variation across the chamber and nozzle. ....	44
Figure 38. Qualitative temperature distribution across the chamber and nozzle. ....	45
Figure 39. Quantitative temperature distribution across the chamber and nozzle. ....	45
Figure 40. Qualitative pressure distribution across the chamber and nozzle. ....	46
Figure 41. Quantitative pressure distribution across the chamber and nozzle. ....	46

## List of Symbols

### Symbols

Symbol	Definition	Units (SI)
$p$	Static pressure of mixture	Pascal
$p_H$	Partial pressure of $H$	Pascal
$p_O$	Partial pressure of $O$	Pascal
$p_{OH}$	Partial pressure of $OH$	Pascal
$p_{H_2}$	Partial pressure of $H_2$	Pascal
$p_{O_2}$	Partial pressure of $O_2$	Pascal
$p_{H_2O}$	Partial pressure of $H_2O$	Pascal
$K_{p,\#}$	Equilibrium constant of chemical reaction	
$N_A$	Avogadro's number	
$N_H$	Number of Hydrogen nuclei	
$N_O$	Number of Oxygen nuclei	
$k$	Reaction rate	
$A$	Frequency factor	
$T$	Temperature	Kelvin
$\beta$	Temperature exponent	
$E_a$	Activation energy	Joules
$R_u$	Universal gas constant	J / (mol. · K)
$M$	Mach number	
$dA, da$	Differential area	m <sup>2</sup>
$u$	Velocity in the x direction	m/s
$v$	Velocity in the y direction	m/s

$v_r, v_g$	Velocity components in conservation of energy equation	m/s
$\rho$	Density	kg/m <sup>2</sup>
$p_e$	Boundary layer edge pressure	Pascals
$S_u, S_E, H, E$	User defined functions	
$q$	Heat transfer	Joules
$f_b$	Body forces	Newtons

# 1. Chapter 1 - Introduction

## 1.1 Motivation

Since the beginning of spaceflight, there has been a desire to develop a cheap, reusable, single-stage to orbit rocket launch vehicle. Such a vehicle was envisioned to make spaceflight more routine and affordable. Over time a variety of designs and systems have been studied to see how best to achieve a single-stage to orbit vehicle. These include an all hydrogen-powered rocket launch vehicle, a combined-cycle jet/rocket engine powered launch vehicle, a combined turbine, ramjet, scram-jet, and rocket powered launch vehicle, and a tripropellant based rocket launch vehicle. In all of these cases the propulsion system was one of the major areas of study and played a primary role in the possible realization of a single-stage to orbit launch vehicle. However, today the single-stage to orbit vehicle is still the long-term dream that it was at the beginning of spaceflight in spite of the myriad advances in launch vehicle technologies. Today the optimal rocket launch vehicle for commercial rocket launches is a two-stage vehicle where the first-stage is powered by a high-density fuel and oxidizer combination, usually kerosene and oxygen, and the second-stage is powered by a low-density fuel and oxidizer combination, usually hydrogen and oxygen (Sutton & Biblarz, 2017). Even with this highly optimized vehicle configuration, the costs of space access remain high. The purpose of the present study is to further investigate and develop the tripropellant rocket launch vehicle concept for the goal of bringing down space access costs. Specifically, a detailed analysis of the combustion properties of a tripropellant rocket engine will be done using computational fluid dynamic simulations. The analysis will help determine the benefits of such an engine to the development of a single-stage to orbit launch vehicle.

## **1.1 Project Proposal**

The objective of this project is to further investigate the performance and capabilities of a tri-propellant rocket engine based on prior research. The main method of analysis would be done through a CFD simulation of a 2-D rocket engine where the combustion process and expansion through a supersonic nozzle will be modeled.

## **2. Chapter 2 - Literature Review**

Before the analysis was done a review of the literature involving tripropellant rocket engines was done in order to understand where the concept stands today. A literature review of the work done in running computational fluid dynamic simulations dealing with rocket engines was also done to better inform and direct the current projects objectives. The following sections summarize the findings of the literature review and what their importance were for the current project.

### **2.1 Basic Rocket Engine Theory**

A review of basic principles of rocket engine theory was done based on the work by Sutton and Biblarz (Sutton & Biblarz, 2017). Nozzle flow for both ideal and real gas conditions were reviewed. Combustion chamber design and thermodynamics were also reviewed. Equilibrium chemistry and reacting flow physics modeling was reviewed from Anderson (Anderson, 2019). Based on a survey of other literature dealing with tripropellant rocket engines specifically and CFD simulation of rocket engines generally, a final CFD setup will be arrived at for the project.

### **2.2 Summary of Previous Research into the Tripropellant Concept**

The subsequent sections present a summary of previously done investigations into the tripropellant rocket engine concept. Each of the studies informed and narrowed the area of investigation to be done for the current study.

#### **2.2.1 Tripropellant Rocket Technology for Reusable Launch Vehicles**

This study was an analysis of a tripropellant rocket engine done by the Chemical Automatics Design Bureau of Russia and Aerojet General Corporation of the U. S. A (Gontcharov

et al, 2004). In this study Gontcharov analyzed the performance of an evolved tripropellant rocket engine based on the Russian RD-0120 rocket engine. This engine was an oxygen-rich staged combustion engine used in the Energia launch vehicle. The proposed engine would have two modes of operation during flight. The first mode, Mode 1, would involve the tripropellant combustion of hydrogen, kerosene, and oxygen for the initial boost phase of flight while the second mode, Mode 2, would involve the bi-propellant combustion of hydrogen and oxygen for the ascent and orbit insertion phase of flight (Gontcharov et al, 2004).

The study initially compared three different configurations for the preburner of the proposed engine: an oxygen-rich preburner, fuel-rich (hydrogen) preburner, and a fuel-rich tripropellant preburner, which mixed hydrogen and kerosene with oxygen. For each preburner the power capability of the generated preburner gas was calculated at temperatures ranging from 850 to 1000 Kelvin. The results showed that the relative power of the preburner gas from the fuel-rich tripropellant preburner was 1.72 to 1.17 times higher than the gas generated by the oxidizer-rich preburner and 1.42 to 1.71 times higher than the gas generated by the fuel-rich (hydrogen) preburner (Gontcharov et al, 2004).

In addition to the preburner comparison, the study also compared the flight RD-0120 engine to a tripropellant demonstration engine. The study looked at various engine characteristics such as the vacuum thrust and specific impulse, sea-level thrust, and specific impulse. The results found that for Mode 1 the vacuum thrust was 134.3 milli-Tons (mT), vacuum specific impulse was 419 seconds, sea-level thrust was 94.5 mT, and sea-level specific impulse was 295 seconds. For Mode 2 the vacuum thrust was 79 mT and vacuum specific impulse was 452 seconds. These were compared to the standard RD-0120 whose vacuum thrust was 200 mT, vacuum specific impulse

was 455.5 seconds, sea-level thrust was 155.6 mT, and sea-level specific impulse was 354 seconds (Gontcharov et al, 2004).

The results found in this study, including both the tripropellant preburner and overall engine characteristics, were a good source to use for the validation of any computational fluid dynamics simulations and will be referenced as needed.

### **2.2.2 Russian Tripropellant Engines for SSTO**

This study looked at using the Russian RD-704 tripropellant rocket engines for a theoretical single-stage to orbit launch vehicle. The study did a trajectory optimization, vehicle sizing, and a parametric study comparing a two-position nozzle with a fixed position nozzle in order to figure out which configuration would have a lower vehicle empty weight.

The end results of the study found that for the two-position nozzle, which had area ratios of 70 and 115, with an overall mixture ratio of 6 and consisted of 6 percent hydrogen the empty weight of the vehicle came to be 212125 pounds (lbs). This was compared to the lower empty weight of 198951 lbs for the fixed nozzle configuration (Vongpaseuth, Venkatasubramanyam, & Martin, 1995).

The engine configuration used in this study, specifically that of the internal configuration of the engine such as the mixture ratios, were a good source to use as a reference when post-processing the results of this projects computational fluid dynamic simulation results.

### **2.2.3 Development of Tripropellant CFD Design Code**

This study looked at a tripropellant CFD design code that had been developed to model local mixing of multiple propellant streams as they are injected into a rocket motor. The code also

served to model bipropellant injectors which was used to validate the accuracy of the code. A three-dimensional kerosene and liquid oxygen injector system was simulated using the model the results of which showed that the flow fields were realistic (Farmer et al, 1997). However, overall the code still needed optimization, but can be used to develop future experiments.

#### **2.2.4 Tripropellant Combustion Process**

This study looked at the effects of introducing hydrogen into the combustion chamber of large liquid oxygen and liquid kerosene rocket engines. Specifically, the additional system stability due to the addition of hydrogen was studied. The study found that the addition of hydrogen improved atomization of the liquid oxygen (Kmiec & Carroll). It also helped to improve combustion efficiency by reducing ignition delays and increasing droplet burning rate and flame speed.

### **2.3 CFD Simulation of a Liquid Rocket Propellant (LH2/Lox) Combustion Chambers**

The next set of studies looked at previously done CFD studies, numerical calculations, and experimental studies of standard liquid hydrogen or kerosene and liquid oxygen combustion chambers. These studies gave a high-level expectation of this study's CFD simulation setup as well as results to validate said setup.

#### **2.3.1 CFD Simulation of a Liquid Rocket Propellant (LH2/Lox) Combustion Chambers**

This study conducted a CFD simulation of the inlet, combustion chamber, and nozzle of an example rocket engine. The simulation used a simple geometry where the combustion chamber length was 4000 milli-meters (mm) and diameter was 3000 mm (Khan et al, 2013). The nozzle followed a parabolic profile for both the convergent and divergent sections and had an area ratio of 25. The propellants were injected into the combustion chamber through seven injector locations.

The combustion of the propellants was modeled based on the Eddy Dissipation Concept and the resulting products expanded through the nozzle (Khan et al, 2013). The simulation results looked at the condition of various parameters such as velocity, static temperature, reaction rates of hydrogen and oxygen, and mass fraction of reactants and products of the combustion reaction. As per theoretical predictions the velocity increases from near zero in the combustion chamber to a maximum of 3500 meters per second (m/s) at the nozzle exit, while the static temperature increases within the combustion chamber and decreases through the throat and nozzle to a low of 2500 Kelvin (Khan et al, 2013). The reaction rates show that the hydrogen and oxygen rates are high in the combustion chamber which results in a low mass fraction of both species near the chamber exit.

Overall this study provided a simple and replicate able CFD simulation for a hydrogen-oxygen rocket engine. The combustion model used in this study, along with the chemical reaction of various species, can be used a reference when validating the combustion model for this project.

### **2.3.2 Numerical Modelling of Liquid Oxygen and Kerosene Combustion at High Pressures**

This study looked at the combustion of liquid oxygen and kerosene at supercritical conditions in an inject for an oxygen-rich preburner through CFD simulation. The simulation was run with ideal gas and real gas modeled thermodynamic properties and compared the results. The simulation used the SST k-w model for turbulence modeling and with the assumption of chemical equilibrium used a probability density function to model the combustion process (Garg et al, 2017). Validation of the simulation was based on validation of the CFD code used and process used. This validation process involved another CFD simulation which replicated experiments performed at MASCOTTE cryogenic combustion test facility using the same CFD setup. A grid independence

study was done with three different grid densities. From this study a medium grid was selected (Garg et al, 2017). The results of the simulation showed that the ideal gas model gave erroneous flame and flow results as compared with experimental data, while the real gas model used gave accurate data compared with experimental data. Overall this study provides a well-developed approach to modeling combustion that can be referenced in this project.

### **2.3.3 CFD Spray Combustion Model for Liquid Rocket Engine Injector Analyses**

This study developed a spray combustion model that accurately modeled the thermodynamic properties of a mixture for a range of pressures and temperature. The model was included into a validated CFD code and used to analyze flow near an injector and subsequently in a combustion chamber and nozzle. The new model was validated by applying it in several testcases that simulated combustion of liquid oxygen and gaseous hydrogen (Cheng & Farmer, 2002). The results of the study showed that the spray model accurately models the combustion process and flow near the injectors.

### **2.3.4 Modelling of Combustion and Heat Transfer in Rocket Combustion Chambers Using CFX**

This paper gave an overview of three different CFD simulations that modeled processes in rocket combustion chambers. The first case looked at the problems involved with using finite rate chemistry in CFD. The second case modeled flow and heat transfer in a porous media. The third case modelled the combustion process in a subscale rocket combustion chamber. The results of the three cases showed that it was possible to model the processes of combustion and heat transfer using the CFX software but that it requires accurate modeling of the main processes taking place in the combustion chamber (Zhukov, 2015).

### **2.3.5 Navier-Stokes Flowfield and Performance Analysis of Liquid Rocket Engines**

In this study another CFD model was developed to model the reacting flows from the combustion chamber through the nozzle and the external plume. The CFD model was applied to the simulation of the Space-Shuttle Main Engine (SSME) but with a modified conical nozzle and the results were compared against actual hot-fire data (Wang & Chen, 1993). The CFD model was a finite difference Navier-Stokes pressure-based, viscous model that assumed equilibrium chemistry (Wang & Chen, 1993). The results of the simulation showed that the calculated specific impulse of the simulated engine match very closely with that measured from the actual engine.

### **2.3.6 Three-Dimensional Numerical Analysis of LOX/Kerosene Engine Exhaust Plume Flow Field Characteristics**

This study ran a three-dimensional CFD simulation of a liquid oxygen and kerosene rocket engine and investigated the resulting plume dynamics. A single-step global chemical reaction and multi-step chemical reaction process is used to model the combustion process of kerosene and oxygen under an equilibrium chemistry assumption. Compressible Reynolds averaged Navier-Stokes equations are used to model the turbulent flow field in the combustion chamber (Cai et al, 2017). A grid independence study was done based on three different meshes; a coarse, medium, and fine mesh. For the study, the medium mesh was used to reduce the necessary computational resources. The end result of the study found that the multi-step chemical reaction modeling is more accurate than the one-step chemical reaction (Cai et al, 2017). This paper will serve as a good reference for the chemical reactions involved in oxygen-kerosene combustion.

### **2.3.7 Subscale Hydrogen/Oxygen Combustion Chamber Experiment**

The study done by Preclik et. al. primarily looked at the combustion chamber wall heat transfer characteristics for a subscale chamber burning liquid hydrogen and oxygen. Their

experimental setup consisted of a 245 mm long combustion chamber with a diameter of 80 mm and a 144 long nozzle section with an area ratio of 5. Liquid hydrogen and liquid oxygen were injected into the combustion chamber through an injector faceplate consisting of 19 coaxial injecting elements. Part of the study also used the experimental tests of the subscale chamber to assess the capability of the CryoROC in-house developed CFD code. A 2-D axisymmetric two-phase simulation was run with the combustion modeled using a dispersed droplet methodology. Turbulence was modeled using standard K-epsilon model. The combustion products were modeled as a real gas. Figure 1 shows the post-processed steady state temperature distribution from the injector face plate to the nozzle exit.

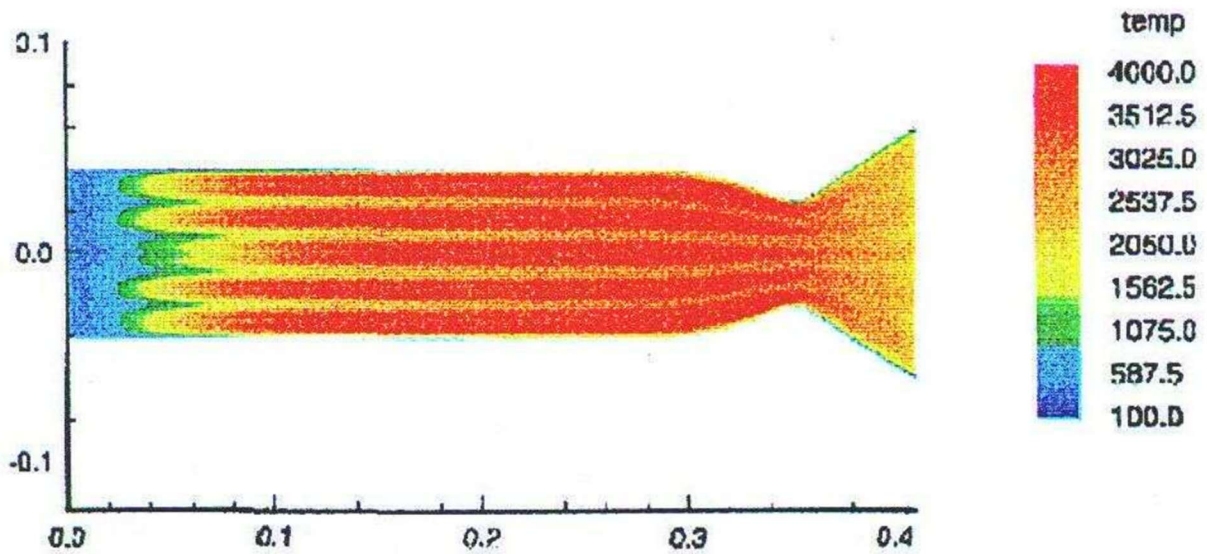


Figure 1. Temperature distribution across combustion chamber and nozzle.

Figure 2 shows the graphical representation of the temperature distribution across the chamber and nozzle.

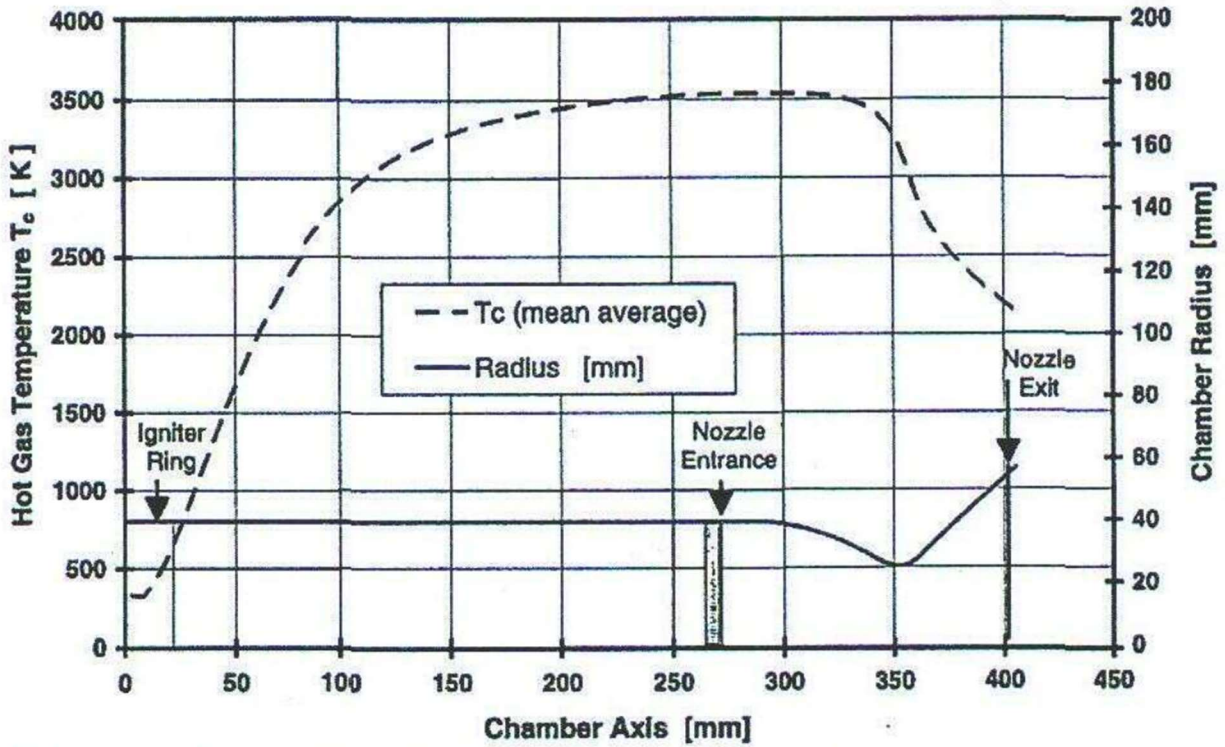


Figure 2. Graphical representation of temperature distribution across combustion chamber and nozzle.

The results shown in Figures 1 and 2 were used as the benchmark for validating the simulation setup that will be used for the tri-propellant combustion study as shown in the subsequent sections.

### **3. Chapter 3 - Methodology**

As an initial step, a simple combustion chamber simulation of hydrogen and oxygen was done. Later this work was extended to replicate a previously done CFD simulation and to simulate and validate past live test fire data. Together these initial steps helped determine combustion and turbulence models, determine necessary chemical reactions, and finalize the mesh and overall CFD setup. With the focus still on combustion simulation, an initial simulation with hydrogen, kerosene, and oxygen was be done. Once convergence and setup issues were resolved, a parametric study was done based on different mixture ratio combinations and their effects on chamber pressures and temperatures.

## 4. Chapter 4 – Theory

Before a CFD simulation of the combustion chamber was done, a thorough investigation of the physics involved in a chemically reacting flow was done. The physics of a combustion chamber simulation involves two distinct phases, a combustion and reacting flow phase and an isentropic expansion phase through a supersonic nozzle. Additionally, boundary layer physics along the chamber and nozzle walls is also considered.

### 4.1 Combustion and Reacting Flow

Generally, the combustion process involves a set of initial reactants which undergo a chemical reaction or a set of reactions at a specific temperature and result in a final set of products. The initial combustion process is unsteady and governed by chemical kinetic theory until steady combustion is achieved where it is governed by chemical equilibrium. The following sections will give an overview of the theories of chemical kinetics and equilibrium chemistry.

#### 4.1.1 Chemical Kinetics

The initial phase of the combustion process is unsteady and governed by chemical kinetic theory. Combustion itself is modeled by relevant chemical reactions that are expected to occur at the specified temperature. Using hydrogen and oxygen as example reactants, Equations 4.1 through 4.4 show some of the possible reactions that can occur (Anderson, 2019).





The above reactions can proceed in both the forward and backward directions and in the initial unsteady phase of combustion the rates at which the forward and backward reactions occur will differ. The reaction rates are commonly determined from the Arrhenius equation, shown in Equation 4.5.

$$k = AT^\beta \exp\left(\frac{-E_a}{R_u T}\right) \quad (4.5)$$

In Equation 4.5,  $R_u$  is the universal gas constant,  $\beta$  is the temperature exponent,  $E_a$  is the activation energy,  $A$  is the frequency factor, and  $T$  is the temperature at which the reaction occurs. As the combustion proceeds and becomes steady, the forward and backward reaction rates for each chemical reaction become more and more equal. At steady state the forward and backward reaction rates are equal and the combustion is in chemical equilibrium.

#### 4.1.2 Equilibrium Chemistry

When the combustion process is modeled as being in chemical equilibrium the forward and backward reaction rates for each chemical reaction are equal. Therefore, the concentration of the reactants and products are steady and constant values. Determining the final state of the combustion chamber after the combustion process involves analytically solving for the equilibrium conditions which involves several steps along with an initial knowledge of the resulting pressure

and temperature, which will be known from the design of the combustion chamber. The end result will provide the exact composition of the resulting mixture of gases in terms of the partial pressures of each species involved in the combustion process.

Using the relevant reactions listed in Equations 4.1 through 4.4, the first step is to determine a relationship between the partial pressures of the individual species involved in the reaction process and the equilibrium constants of each reaction, denoted as  $K_p$ , as shown in equations 4.6 through 4.9.

$$\frac{p_H}{\sqrt{p_{H_2}}} = K_{p,1} \quad (4.6)$$

$$\frac{p_O}{\sqrt{p_{O_2}}} = K_{p,2} \quad (4.7)$$

$$\frac{p_{OH}p_H}{p_{H_2}p_O} = K_{p,3} \quad (4.8)$$

$$\frac{p_{H_2O}}{p_{OH}p_H} = K_{p,4} \quad (4.9)$$

The equilibrium constants indicate the likelihood of the specific reaction occurring at the given temperature. This value is found in several ways, but the most common is to reference tables of thermochemical equilibrium properties of each species in the reaction. Such information has been experimentally determined and is freely available for access. However, with the known equilibrium constants there is still not enough information to determine the partial pressures of all species.

The second step is to satisfy Dalton's law of partial pressures shown in Equation 4.10 (Anderson, 2019).

$$p_{H_2} + p_H + p_{O_2} + p_O + p_{OH} + p_{H_2O} = p \quad (4.10)$$

Dalton's law relates the partial pressures of the individual species involved in the combustion process to the pressure of the overall mixture, which is a known quantity.

The third step involves relating the ratio of the number of nuclei of atoms involved in the combustion process. In this example, the ratio between the number of hydrogen and oxygen atoms is a known quantity and relates to the partial pressures of each species involved in the combustion process as shown in Equation 4.11 (Anderson, 2019).

$$\frac{N_H}{N_O} = \frac{N_A(2p_{H_2} + p_H + 2p_{H_2O} + p_{OH})}{N_A(2p_{O_2} + p_O + 2p_{H_2O} + p_{OH})} \quad (4.11)$$

With the equilibrium constant equations, Dalton's law, and the ratio of atoms, there are now enough equations to solve simultaneously to obtain the partial pressures of each species in the combustion process. With the partial pressures, known the combustion process is fully modeled and various other thermodynamic properties, such as enthalpy, gas mixture pressure, and temperature can be derived (Sutton & Biblarz, 2017). These derived thermodynamic properties determine the state of the reservoir conditions near the exit of the combustion chamber and will be important in the process of isentropic expansion through a supersonic nozzle.

## 4.2 Isentropic Expansion

The combustion process results in the formation of a high temperature and pressure gas mixture consisting of the products of the various chemical reactions that occur in the combustion chamber. The overall purpose of the rocket engine is to generate thrust and this is done by expanding the high temperature and pressure gas mixture through a supersonic nozzle. For simplicity, it is generally assumed that the flow of gas through the supersonic nozzle is no longer chemically reacting. This assumption is known as frozen chemistry assumption and it results in certain conditions of the flow remaining constant such as the specific heat of pressure and volume and by extension their ratio. Entropy is also constant and so the flow is considered as isentropic. For a steady, inviscid, adiabatic, quasi-one-dimensional flow a relation can be derived relating the speed of the flow to the variation in cross-sectional area of a nozzle as shown by Equation 4.12.

$$\frac{dA}{A} = (M^2 - 1) \frac{du}{u} \quad (4.12)$$

In Equation 4.12  $M$  is the Mach number of the flow,  $u$  is the flow velocity, and  $A$  is the cross-sectional area of the nozzle. Equation 4.12 shows that for subsonic flow, where  $M < 1$ , the flow velocity will only increase as the cross-sectional area decreases, that is as the area converges. For supersonic flow, where  $M > 1$ , the flow velocity will only increase as the cross-sectional area increases, that is as the area diverges. Figure 3 shows the basic schematic of a supersonic nozzle and how the Mach number varies through the nozzle.

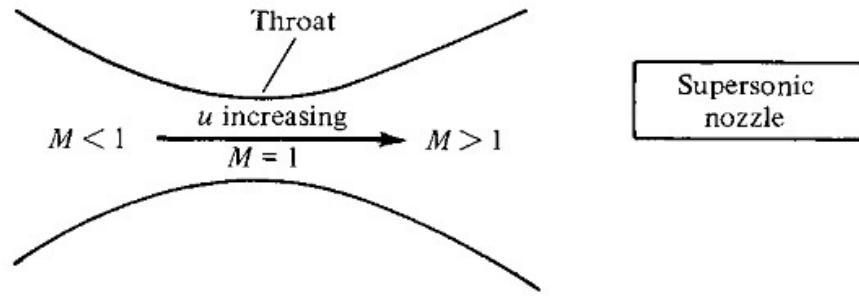


Figure 3. Schematic of a supersonic nozzle.

As the flow through the nozzle reaches a steady state a sonic condition is established at the region of the nozzle with the smallest cross-sectional area, also known as the throat. The nozzle is said to be choked in this throat region as the flow transitions from subsonic to supersonic and so information about the flow cannot travel upstream of the throat. Though above discussion has focused on inviscid flow, in reality the flow both in the nozzle, as well as the combustion chamber is viscous and so will result in the formation of boundary layers. The flow behavior within these boundary layers is discussed in the next section.

### 4.3 Boundary Layer Flow

The flow near the walls of the combustion chamber and nozzle is viscous and results in the formation of boundary layers. The flow outside of the boundary layer can be treated as inviscid, but the flow within the boundary layer is governed by the boundary layer equations shown in Equations 4.13 through 4.15.

$$\frac{\partial(\rho u)}{\partial x} + \frac{\partial(\rho v)}{\partial y} = 0 \quad (4.13)$$

$$\rho u \frac{\partial u}{\partial x} + \rho v \frac{\partial u}{\partial y} = \frac{-dp_e}{dx} + \frac{\partial}{\partial y} \left( \mu \frac{\partial u}{\partial y} \right) \quad (4.14)$$

$$\rho u \frac{\partial h}{\partial x} + \rho v \frac{\partial h}{\partial y} = \frac{\partial}{\partial y} \left( k \frac{\partial T}{\partial y} \right) + u \frac{dp_e}{dx} + \mu \left( \frac{\partial u}{\partial y} \right)^2 \quad (4.15)$$

Equation 4.13 is the continuity equation for two-dimensional flow where  $\rho$  is the density of the fluid and  $u$  and  $v$  are the flow velocities along the  $x$  and  $y$  directions, respectively.

Equation 4.14 is the conservation of momentum equation along the  $x$  direction, where  $\mu$  is the dynamic viscosity of the fluid and  $p_e$  is the pressure at the edge of the boundary layer. Finally,

Equation 4.15 is the conservation of energy equation, where  $h$  is the enthalpy,  $k$  is the thermal conductivity, and  $T$  is the temperature. The formation of boundary layers is a result of the fact that the flow velocity at the boundary of the body, in this case the nozzle walls, is zero, while at the edge of the boundary layer the flow velocity equals the freestream velocity. This velocity gradient is shown in Figure 4.

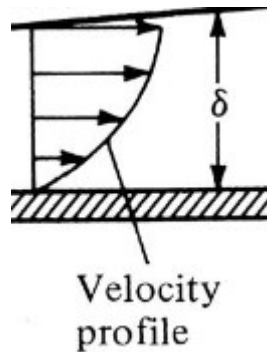


Figure 4. Velocity gradient within the boundary layer.

The combination of reacting flow, isentropic expansion, and boundary layer flow will play a role in the overall description of the flow field in the rocket engine combustion chamber and nozzle and is the subject of the next chapter.

## 5. Chapter 5 – Governing Equations

Star CCM+ was the software tool used to run CFD simulation of the rocket engine combustion chamber and nozzle. The governing equations that Star CCM+ solves over a finite control volume to determine the various thermodynamic and fluid properties are as follows:

$$\frac{\partial}{\partial t} \int_V \rho dV + \oint_A \rho v \cdot da = \int_V S_u dV \quad (5.1)$$

$$\frac{\partial}{\partial t} \int_V \rho v dV + \oint_A \rho v \times v \cdot da = - \oint_A p I \cdot da + \oint_A T \cdot da + \int_V f_b dV + \int_V S_u dV \quad (5.2)$$

$$\begin{aligned} \frac{\partial}{\partial t} \int_V \rho E dV + \oint_A [\rho H v_r + v_g p] \cdot da \\ = - \oint_A q'' \cdot da + \oint_A T \cdot v da + \int_V f_b \cdot v dV + \int_V S_E dV \end{aligned} \quad (5.3)$$

Equation 5.1 represents the conservation of mass of the flow through the control volume. The first term is the time rate of increase of mass inside of the control volume, while the second term is the net mass flow out of the control volume. Finally, the third term, on the right-hand side of Equation 5.1, is a user source term.

Equation 5.2 represents the conservation of momentum of the flow through the control volume. The first term is the rate of change of momentum within the control volume, while the second term is the momentum flux across the control surface. The third, fourth, and fifth terms, on the right-hand side of Equation 5.2, represent the surface and body forces acting on the

control volume. The surface forces include the pressure distribution and the shear and normal stress distributions over the surface of the control volume. Finally, the sixth term is a user source term.

Equation 5.3 represents the conservation of energy of the flow through the control volume. The left-hand side of Equation 5.3 denotes the rate of change of energy within the control volume. This is a combination of the change in the internal energy, first term, and kinetic energy, second term, of the fluid in the control volume. The third term beginning on the right-hand side of Equation 5.3 is the net flux of heat into the control volume. The fourth and fifth terms together represent the rate of work done on the control volume due to body and surface forces. Finally, the sixth term is a user source term.

The system of equations that Equations 5.1 through 5.3 constitute are not enough to fully solve for all properties of the flow as the number of unknowns exceeds the number of equations. To be able to find a complete solution of the flow field, an additional equation is needed. This additional equation is the equation of state:

$$p = \rho RT \quad (5.4)$$

In Equation 5.4  $R$  is the ideal gas constant of the resulting mixture of gases produced by the combustion process and  $T$  is the temperature. Equations 5.1 through 5.4 are solved simultaneously through numerical methods by the Star CCM+ software to determine the properties of the flow in a CFD simulation. An overview of the code and numerical methods is discussed in the next chapter.

## 6. Chapter 6 – CFD Code Overview

In order to solve the governing equations from Chapter 5, Star CCM+ discretizes the continuous system of equations into a set of discrete algebraic equations. The general discretization process begins by dividing up the domain of the equations into a finite number of cells and elements. The next step involves storing the unknown fluid properties at specific locations in the mesh. Star CCM+ specifically uses a co-located variable arrangement, which means that the unknowns are stored at the cell center of each cell in the mesh. Finally, the last step is solving the coupled system of algebraic equations numerically at each time step of the simulation. Because the set of algebraic equations are non-linear, they are solved iteratively.

### 6.1 Solver Settings

Figure 5 shows the general settings used when simulating a reacting flow, such as that found in the combustion chamber and nozzle of a rocket engine.

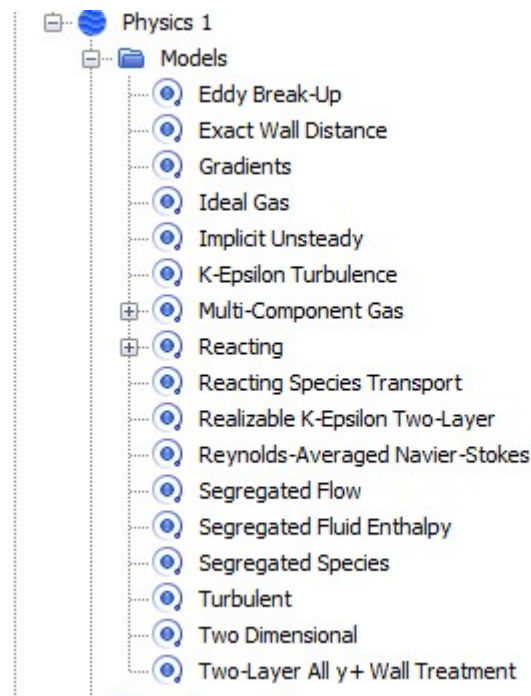


Figure 5. Physics set up of the simulation.

### **6.1.1 Two Dimensional**

A rocket combustion chamber and nozzle maybe symmetrical and therefore lend itself to an axisymmetric setup. Although it would not be as accurate as a three-dimensional simulation due to inability of flow to cross the center line, it would be accurate enough to represent the interactions of the flow in the entire domain as well as being computationally less intensive.

### **6.1.2 Unsteady, Segregated Flow, and Segregated Enthalpy**

An implicit, or unsteady, segregated flow solver is used to solve the momentum equation for each direction in turn. The segregated flow uses a predictor-corrector approach to link the momentum and continuity equations. A segregated fluid enthalpy setup is used to solve the energy equation. It uses the chemical thermal enthalpy as the solved variable and calculates the temperature from the enthalpy using the equation of state.

### **6.1.3 Reacting Species Transport, Eddy Break-Up, Multi-Component Gas, Segregated Species**

Reacting flow, specifically combustion, is modeled in Star CCM+ using the Reacting Species Transport setup, which solves for the mass fractions of all species involved in the chemical reactions that characterize combustion. The Eddy Break-Up sub-model of the Reacting Species Transport model is used to simulate the simple one or two step chemical reactions. It is useful for modeling chemistry where the reaction rate is determined by the rate at which turbulence can mix the reactants. The details of what species are involved in the chemical reactions is outlined by the Multi-Component Gas option. With this option different chemical reactions can be modeled by specifying the reactants, products, and their associated

stoichiometric coefficients. The Segregated Species model further defines the convection scheme to be used in simulation. For computational simplicity, a first order upwind convection scheme will be used in most simulations.

#### **6.1.4 Reynolds-Averaged Navier-Stokes, Standard K-Epsilon, K-Epsilon Turbulence**

The turbulence model implemented by Star CCM+ and used in subsequent simulations is the Reynolds-Averaged Navier-Stokes (RANS) model. This model finds an approximate solution to the Reynolds-Averaged Navier-Stokes equations. Specifically, the K-Epsilon sub-model will be used. This turbulence model is a two-equation model that solves the transport equations for the turbulent kinetic energy and turbulent dissipation rate in order to determine the turbulent eddy viscosity which is then used to solve the RANS equations.

The above specified solver settings will be used to model and analyze the flow in the combustion chamber and nozzle of a simple rocket engine.

## 7. Chapter 7 – Validation Test Case

### 7.1 Testcase

Before attempting a full combustion chamber CFD simulation where the combustion characteristics of hydrogen, oxygen, and kerosene at different mixtures is examined, a test-case CFD simulation was run in order to validate the simulation setup and basic combustion chemistry. The validation test-case replicated the results obtained by the study done by Preclik et. al. on a subscale combustion chamber and the combustion of hydrogen and oxygen.

#### 7.1.1 Geometry

The basic geometry is shown in Figure 6. It is a 2-D geometry composed of 3 injector sections, a wall section, a symmetry plane, and a nozzle exit section. The length of the geometry from the injector to nozzle exit is 384 mm while the nozzle exit diameter is 46 mm.



Figure 6. 2D Geometry.

#### 7.1.2 Mesh

Figure 7 shows the unstructured quadrilateral mesh generated for the 2-D geometry. The automated mesh generation (2D) tool in Star-CCM+ was used to generate a coarse mesh (“Star-CCM”).

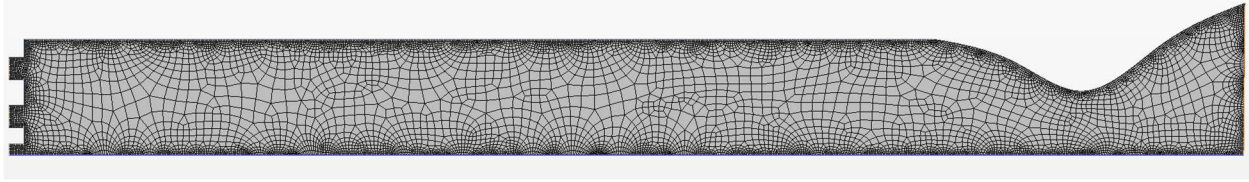


Figure 7. Generated mesh.

Figure 8 shows a detailed view of the mesh near the injector and wall regions of the geometry. Because of the viscous nature of the flow the mesh near the boundaries of the geometry were made to be finer in order to more accurately resolve features such as boundary layers.

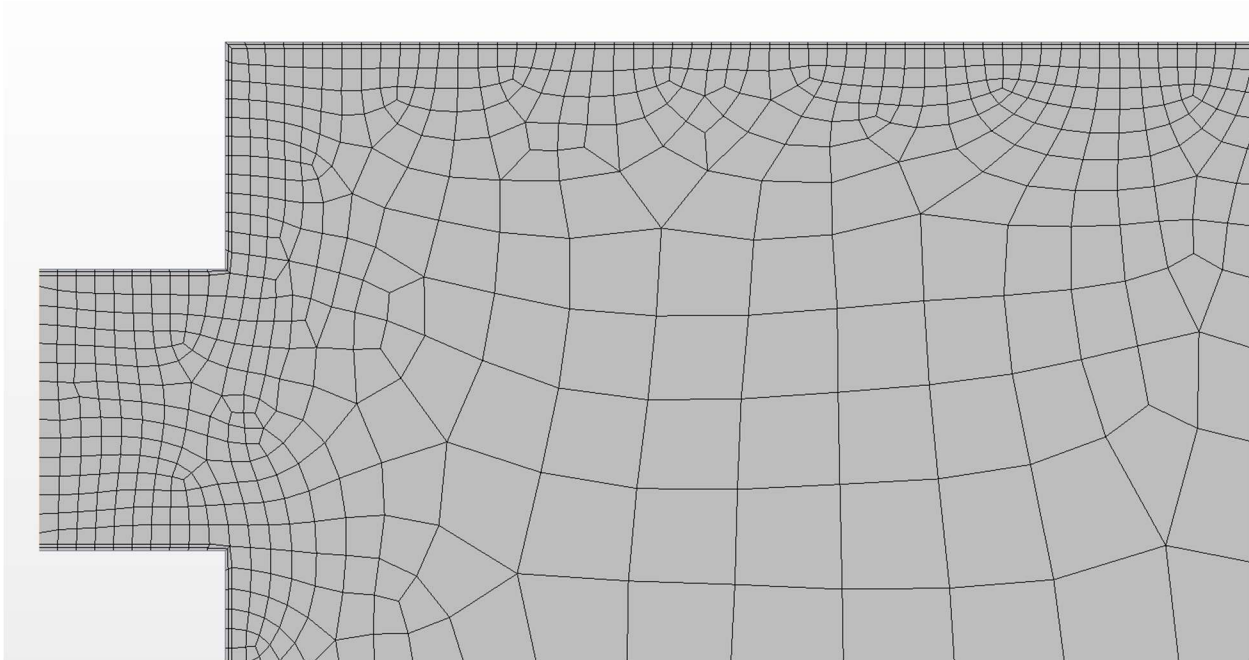


Figure 8. Mesh detail near the boundaries of the geometry.

### 7.1.3 Simulation

A multi-component gas model was used involving  $O_2$ ,  $H_2$ ,  $H_2O$ , and Air. A single-step reaction was used to model the combustion with the stoichiometric coefficients of  $O_2$ ,  $H_2$ , and  $H_2O$

of 0.5, 1, and 1, respectively. The initial conditions of the simulation were that the pressure in the rocket engine was at 101325 pascals and the initial temperature was 300 Kelvin. The fuel and oxidizer entered into the combustion chamber through the injector sections. The fuel inlet boundaries were on the top and bottom sides of the injectors and were set to have a mass inflow rate of 0.6325 kg/s each. The oxidizer inlet mass flow rate was set to 6.8 kg/s. The simulation was set to run for 20000 steps in order to allow enough time for the combustion reaction to achieve equilibrium conditions and for the resulting flow to become steady.

#### 7.1.4 Results

Figure 9 shows a cross-sectional visual view of the simulation results. It shows the temperature distribution from the injectors to the nozzle exit. Figure 10 shows the graphical representation of this temperature distribution.

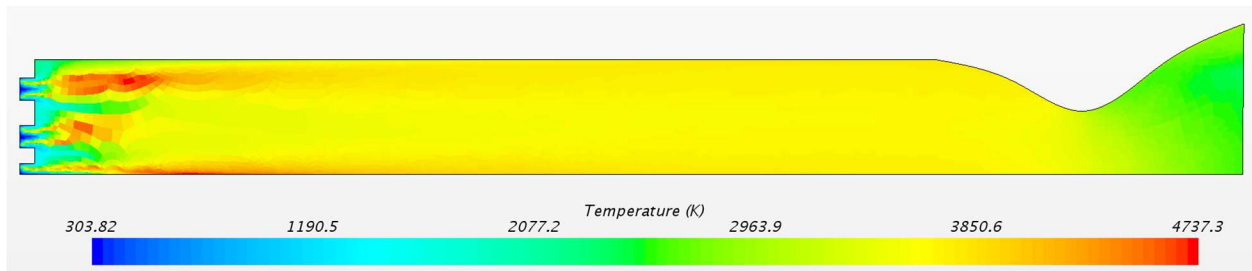


Figure 9. Temperature variation from combustion chamber to nozzle exit.

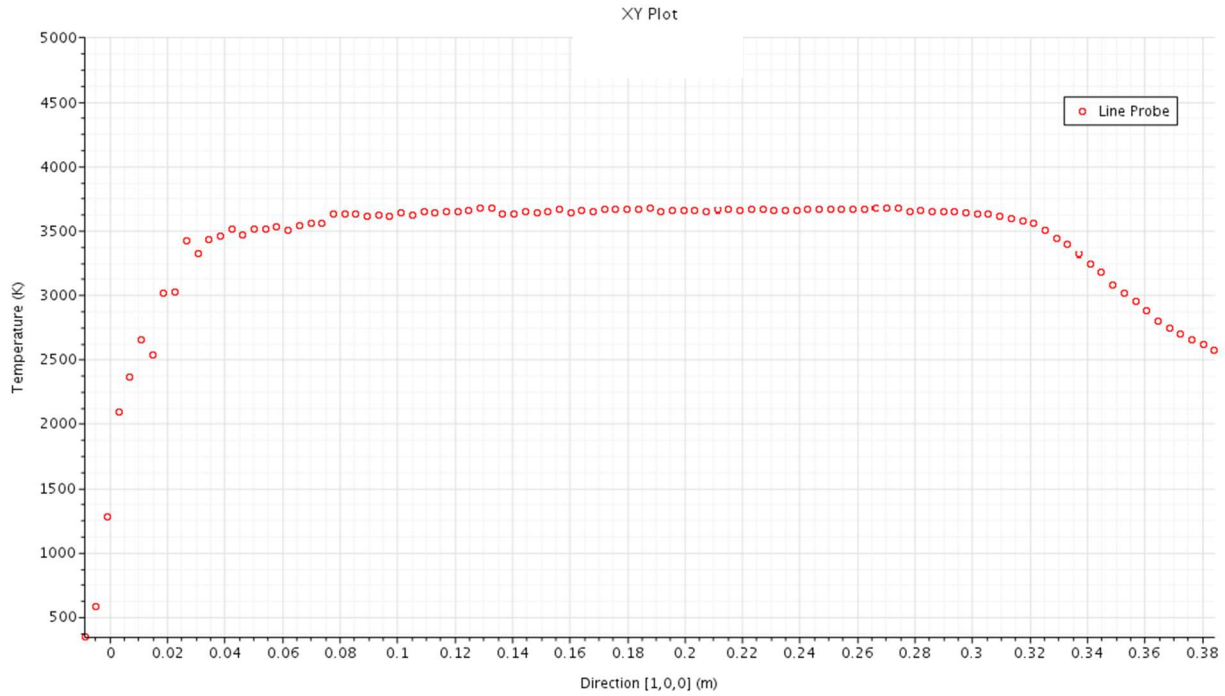


Figure 10. Graphical representation of temperature variation from combustion chamber to nozzle exit.

Comparing the results shown in Figure 10 with those shown in Figure 5, it can be seen that the simulation matches very closely with the results of Prelik et. al. In both cases the temperature rises from around 500 K to a little over 3500 K as the fuel and oxidizer are injected into the combustion chamber and combust. The hot gaseous products then flow down the combustion chamber and are expanded through the converging diverging nozzle which results in the temperature dropping to around 2500 K. The matching temperature distribution between the simulation and previously done simulations show that the simulation setup provides an accurate representation of the combustion process.

## **8. Chapter 8 – Tripropellant Simulation**

With a baseline established for the simulation environment and settings, an investigation on the effects of introducing an additional fuel, kerosene, into the combustion process was done. The initial steps were to determine how the kerosene will be introduced into the combustion chamber and what chemical reaction was to be used to model the combustion of kerosene and oxygen. Once this was done four different combustion scenarios were looked at. In the first scenario, hydrogen and kerosene were introduced into the chamber at the same mass flow rate. In the second scenario kerosene was introduced into the chamber at a higher mass flow rate than hydrogen. In the third scenario hydrogen was introduced into the chamber at a higher mass flow rate than kerosene. Finally, in the fourth scenario hydrogen and kerosene were introduced at the same mass flow rate, but the oxygen mass flow rate was increased. After gathering the simulation data for each scenario, a discussion and comparison of the results was done.

### **10.1 Kerosene Injection Configuration**

The first step in the investigation was to determine how the kerosene will be introduced into the combustion chamber. Figure 11 shows the details of one of the three injector regions of the overall geometry.

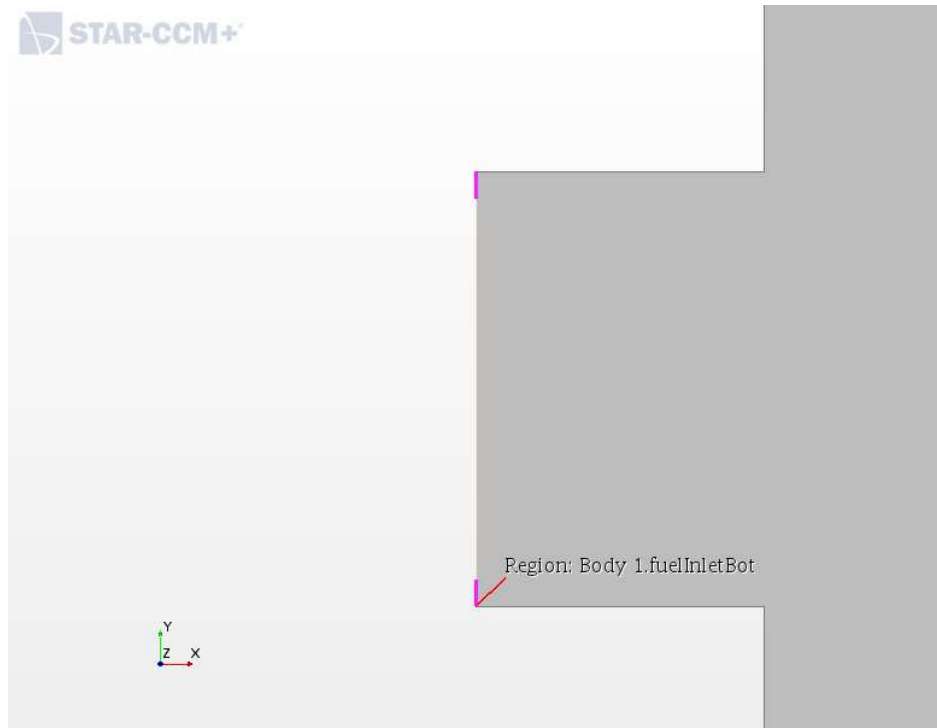


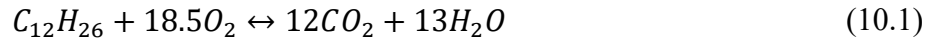
Figure 11. Injector region.

Hydrogen enters the combustion chamber through channels on the top and bottom portion of the injector, while oxygen enters from the central portion. The selection of where and how kerosene enters the combustion chamber would normally be based on how best to optimally mix it with hydrogen and oxygen however, because the primary interest of this study is the combustion chemistry of tripropellant systems a simpler arbitrary selection was made. The bottom channels, which injected hydrogen, were changed so that kerosene was instead injected. The final tripropellant injector configuration was such that hydrogen enters the combustion chamber through the top channel, oxygen enters through the central surface, and kerosene enters through the bottom channel.

## 10.2 Kerosene and Oxygen Chemical Reaction

Because a single step reaction was used to model the combustion of hydrogen and oxygen in the validation testcase, a similar setup was used to model the combustion of kerosene and

oxygen. Equation 10.1 shows the chemical equation used to represent this combustion (Garg et al, 2017).



### 10.3 Scenario 1: Matching Hydrogen and Kerosene Mass Flow Rates

In this scenario the same simulation setup as the validation testcase was used with the main difference being that the bottom fuel injectors outputted kerosene. The hydrogen and kerosene mass flow rates were kept the same at 0.6325 kg/s, while the oxygen mass flow rate was kept at 6.8 kg/s.

#### 10.3.1 Mole Concentration of Reactants and Products

Figures 12 through 14 show the variation in the concentrations of the reactants of combustion; hydrogen, oxygen, and kerosene.

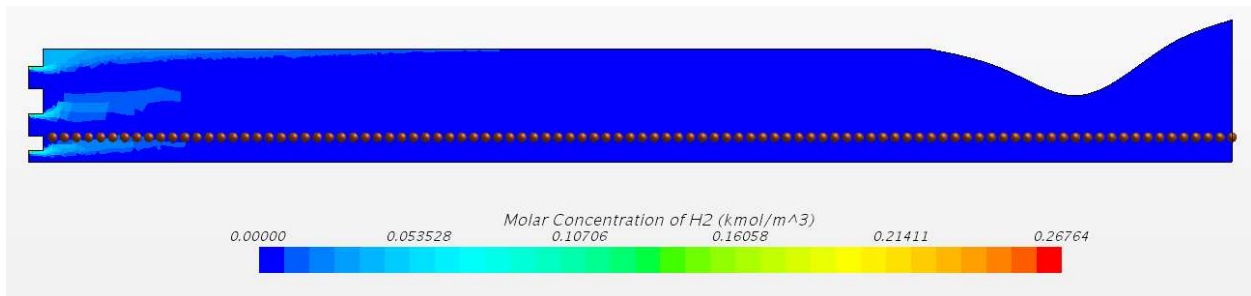


Figure 12. Hydrogen concentration variation across the chamber and nozzle.

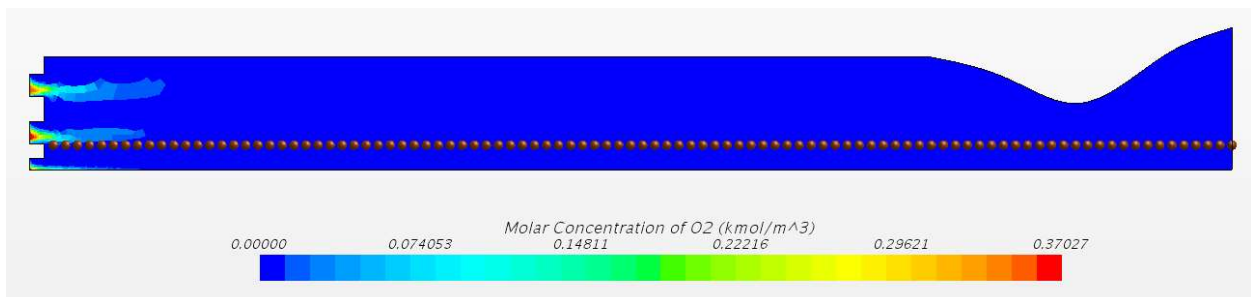


Figure 13. Oxygen concentration variation across the chamber and nozzle.

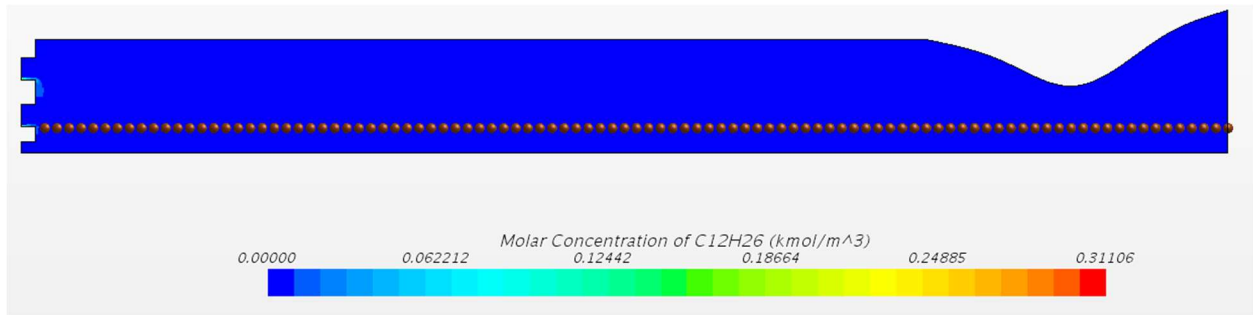


Figure 14. Kerosene concentration variation across the chamber and nozzle.

Figures 15 and 16 show the variation in the concentrations of the products of combustion: water and carbon-dioxide.

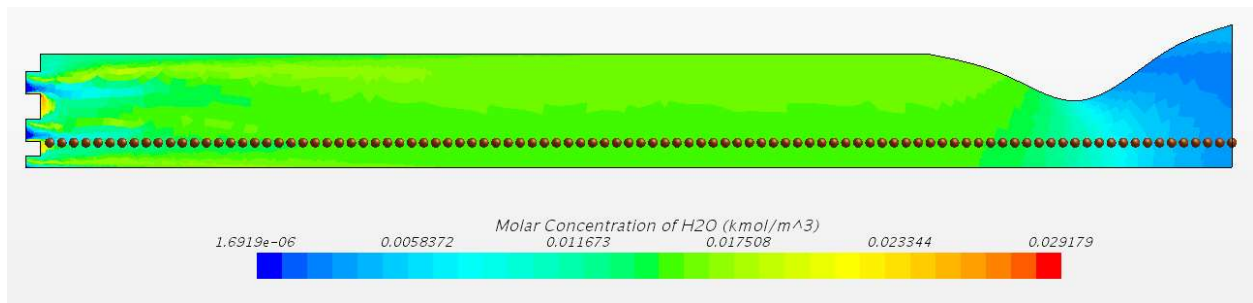


Figure 15. Water concentration variation across the chamber and nozzle.

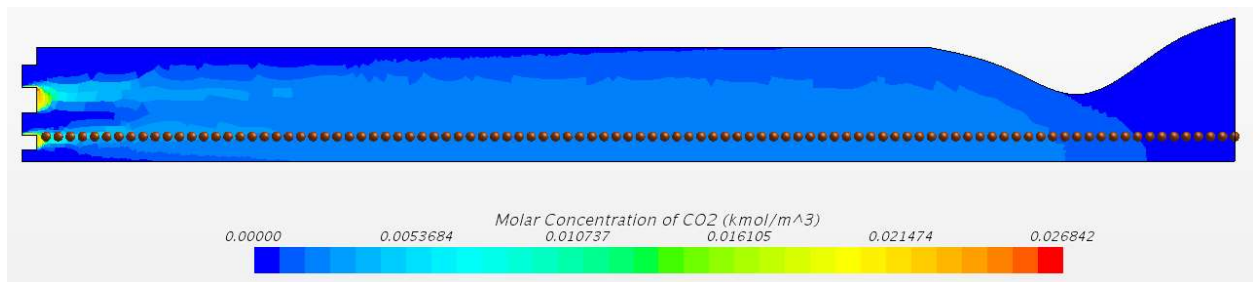


Figure 16. Carbon-dioxide concentration variation across the chamber and nozzle.

As can be seen from Figures 12 and 14, although the hydrogen and kerosene had the same mass flow rate, the concentration of hydrogen was higher and the presence of hydrogen lasted for a longer distance into the combustion chamber than kerosene. This is mainly due to the fact that hydrogen has a far lower density than kerosene and for the same mass flow rate and

inlet surface area the in-flow velocity of hydrogen is higher than kerosene. Similarly, the concentration and presence of oxygen was much higher than either fuel due to the higher mass flow rate. Figures 15 and 16 show that the full combustion of hydrogen, oxygen, and kerosene occurs by the end of the first third of the combustion chamber after which the concentration of water and carbon-dioxide dominates the mixture.

### 10.3.2 Temperature and Pressure Distribution

Figures 17 and 18 show the qualitative and quantitative temperature distribution across the combustion chamber and nozzle.

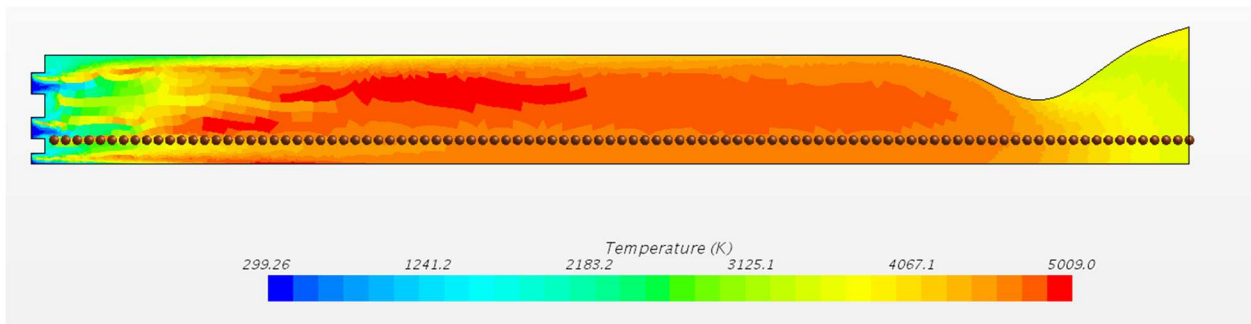


Figure 17. Qualitative temperature distribution across the chamber and nozzle.

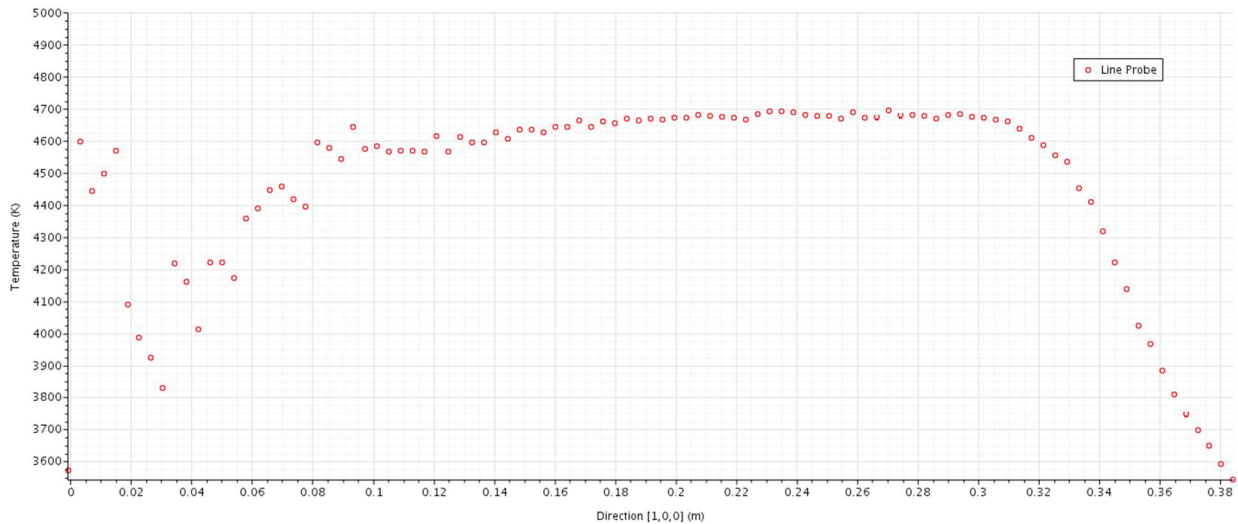


Figure 18. Quantitative temperature distribution across the chamber and nozzle.

The temperature profile shown in Figure 18 is measured along the dotted probe line shown in Figure 17. Both figures show that the temperature increases from near 100 K to a steady 4700 K and then drops as the hot gaseous mixture is expanded through the supersonic nozzle. The temperature stabilizes at around a 100 mm into the combustion chamber and begins to drop at around the 320 mm mark.

Figures 19 and 20 show the qualitative and quantitative pressure distribution across the combustion chamber and nozzle.

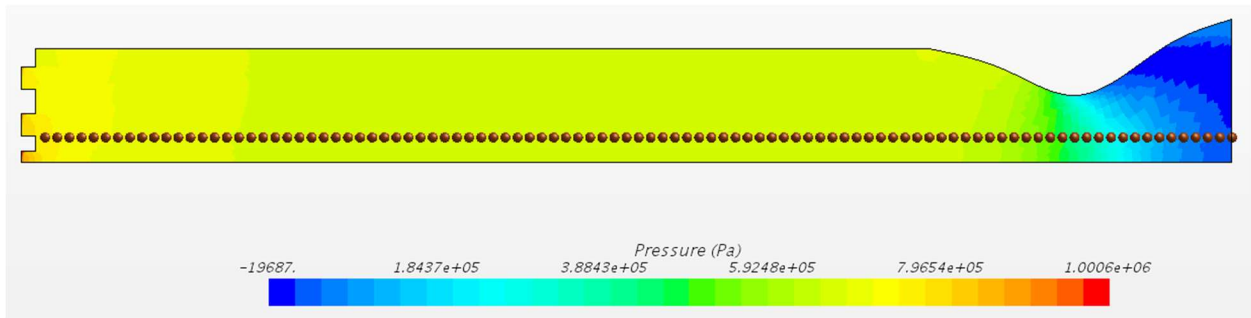


Figure 19. Qualitative pressure distribution across the chamber and nozzle.

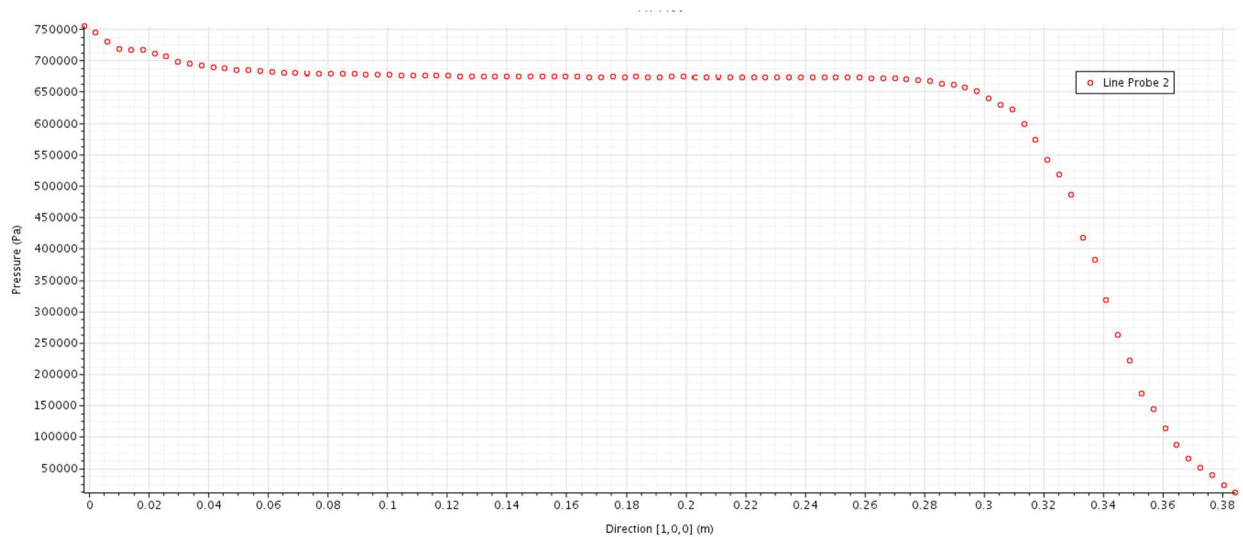


Figure 20. Quantitative pressure distribution across the chamber and nozzle.

The pressure profile shown in Figure 20 is measured along the dotted probe line shown in Figure 19. Both figures show that the pressure stabilizes quickly to around 675 KPa after which it decreases drastically as the gaseous mixture is expanded through the supersonic nozzle. The initial pressure in the graph in Figure 20 is high because the probe line begins somewhat within the combustion chamber. This initial pressure is also higher than the stabilized value later in the chamber due to the initiation of combustion in the initial part of the chamber.

#### 10.4 Scenario 2: Higher Kerosene Mass Flow Rate than Hydrogen

In this scenario the kerosene mass flow rate was doubled to 1.265 kg/s while the hydrogen and oxygen mass flow rate were kept same at 0.6325 kg/s and 6.8 kg/s, respectively.

##### 10.4.1 Mole Concentration of Reactants and Products

Figure 21 shows the new variation in the concentration of kerosene.

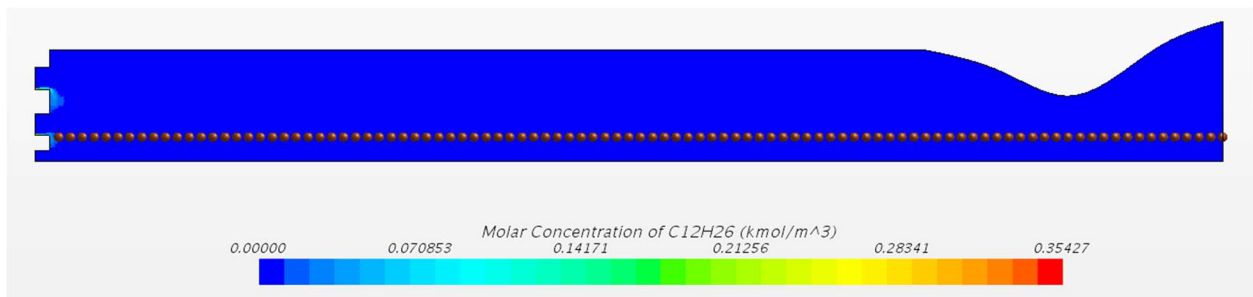


Figure 21. Kerosene concentration variation across the chamber and nozzle.

Figures 22 and 23 show the variation in the concentrations of the products of combustion: water and carbon-dioxide.

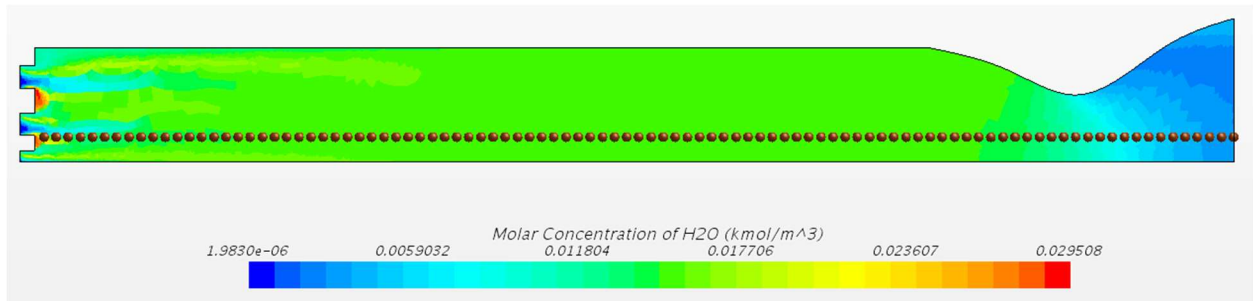


Figure 22. Water concentration variation across the chamber and nozzle.

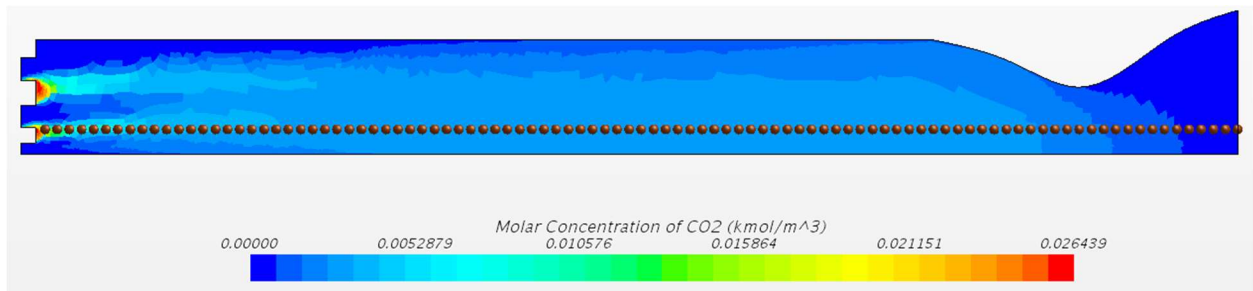


Figure 23. Carbon-dioxide concentration variation across the chamber and nozzle.

As can be seen from Figure 21 the concentration of kerosene is marginally higher near the injector region and the presence of kerosene lasts longer into the combustion chamber. The concentrations of hydrogen and oxygen do not change as much as they have the same mass flow rate as before. Figures 22 and 23 show that the full combustion of hydrogen, oxygen, and kerosene still occurs by the end of the first third of the combustion chamber after which the concentration of water and carbon-dioxide dominates the mixture. Comparing the concentrations of water and carbon-dioxide between scenario 2 and scenario 1, there is a slight increase in the initial concentrations of both products in scenario 2 due to the increased mass flow rate of kerosene.

## 10.4.2 Temperature and Pressure Distribution

Figures 24 and 25 show the qualitative and quantitative temperature distribution across the combustion chamber and nozzle.

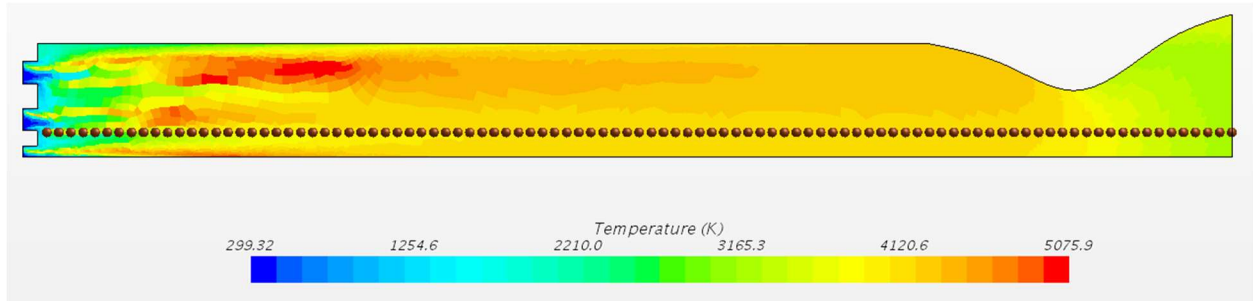


Figure 24. Qualitative temperature distribution across the chamber and nozzle.

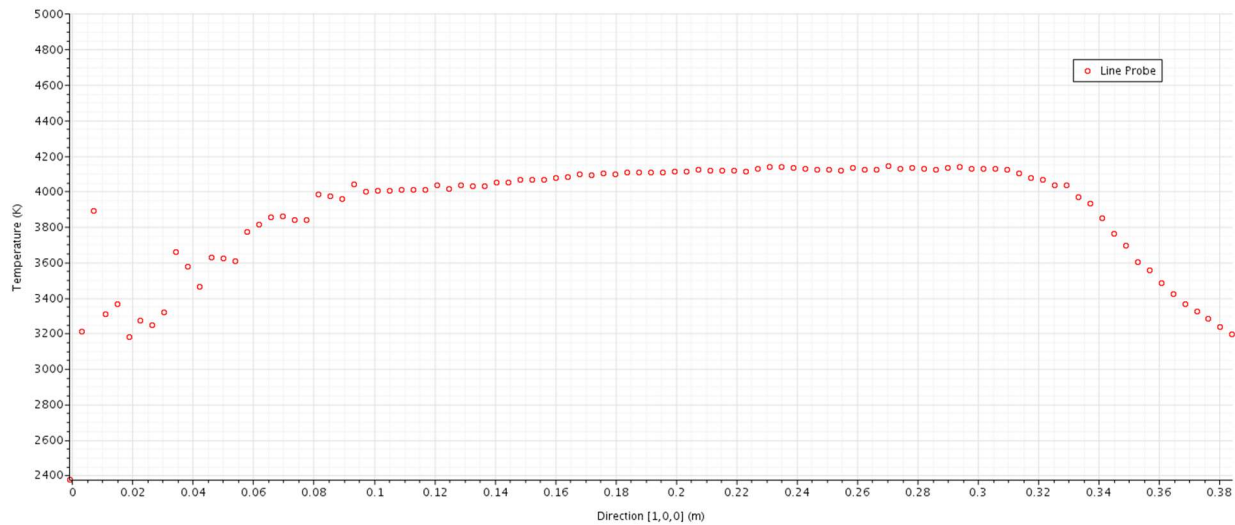


Figure 25. Quantitative temperature distribution across the chamber and nozzle.

Both figures show that the temperature increases from near 100 K to a steady 4100 K and then drops as the hot gaseous mixture is expanded through the supersonic nozzle. The temperature stabilizes at around a 100 mm into the combustion chamber and begins to drop at around the 320 mm mark. Comparing the temperature distribution graph between scenario 2 and scenario 1, it can be seen that increasing kerosene mass flow rate has decreased the overall achieved

combustion chamber temperature. This is primarily due to the fact that there is now more kerosene to be burned, but with the same oxygen supply. Thus, the gaseous mixture is now more kerosene-rich and so the overall temperature is lower.

Figures 26 and 27 show the qualitative and quantitative pressure distribution across the combustion chamber and nozzle.

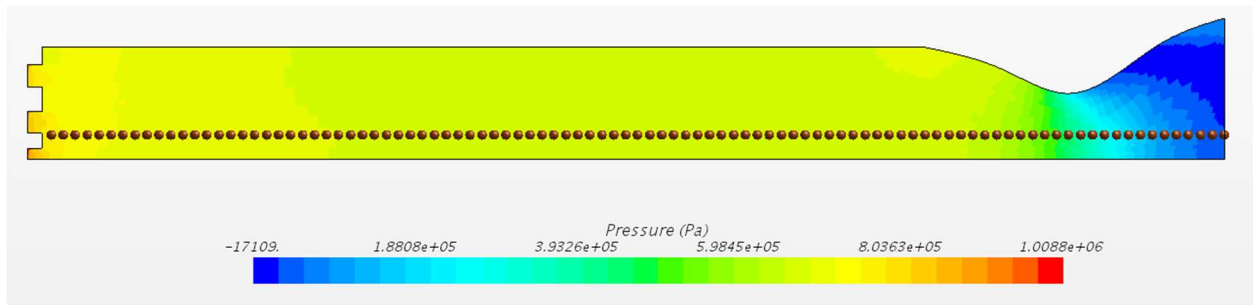


Figure 26. Qualitative pressure distribution across the chamber and nozzle.

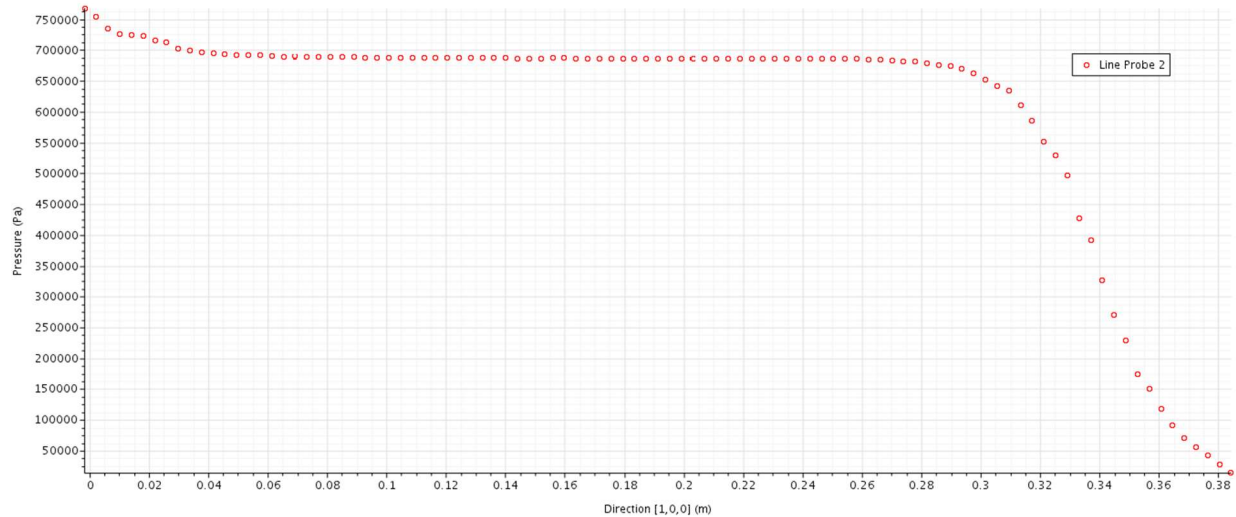


Figure 27. Quantitative pressure distribution across the chamber and nozzle.

Both figures show that the pressure stabilizes quickly to around 690 KPa after which it decreases drastically as the gaseous mixture is expanded through the supersonic nozzle. Comparing the

pressure graphs between scenario 2 and scenario 1, it can be seen that increasing the kerosene mass flow rate has increased the overall pressure within the combustion chamber.

### 10.5 Scenario 3: Higher Hydrogen Mass Flow Rate than Kerosene

In this scenario the hydrogen mass flow rate was doubled to 1.265 kg/s while the kerosene and oxygen mass flow rate were set to 0.6325 kg/s and 6.8 kg/s, respectively.

#### 10.5.1 Mole Concentration of Reactants and Products

Figure 28 shows the new variation in the concentration of hydrogen.

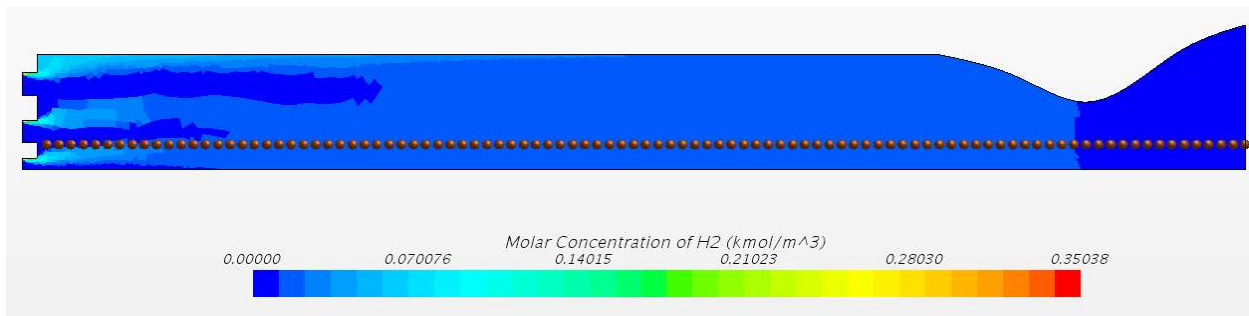


Figure 28. Hydrogen concentration variation across the chamber and nozzle.

Figures 29 and 30 show the variation in the concentrations of the products of combustion: water and carbon-dioxide.

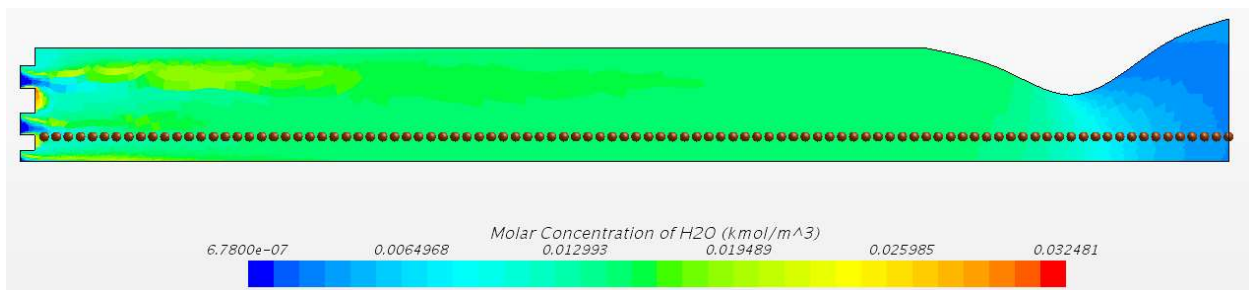


Figure 29. Water concentration variation across the chamber and nozzle.

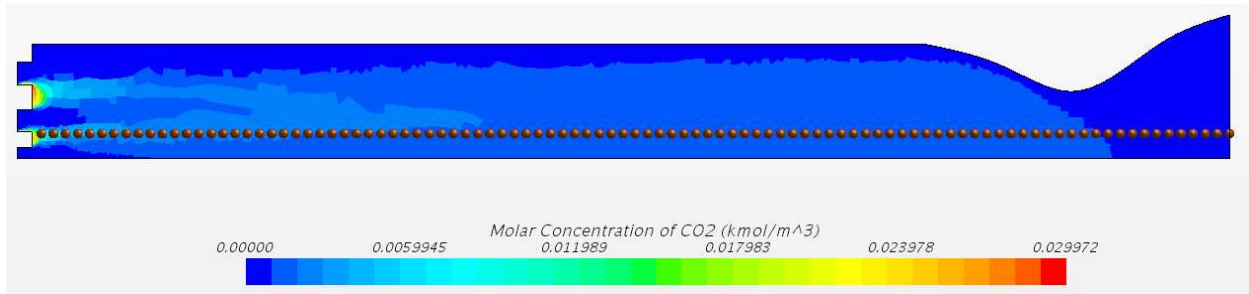


Figure 30. Carbon-dioxide concentration variation across the chamber and nozzle.

As can be seen from Figure 28 the concentration of hydrogen is marginally higher near the injector region and the presence of hydrogen lasts longer into the combustion chamber. The concentrations of kerosene and oxygen do not change as much as they have the same mass flow rate as before. Figures 29 and 30 show that the full combustion of hydrogen, oxygen, and kerosene still occurs by the end of the first third of the combustion chamber after which the concentration of water and carbon-dioxide dominates the mixture. Comparing the concentrations of water and carbon-dioxide between scenario 3 and scenarios 1 and 2, there is a measurable increase in the initial concentrations of water in scenario 3 due to the increased mass flow rate of hydrogen.

### 10.5.2 Temperature and Pressure Distribution

Figures 31 and 32 show the qualitative and quantitative temperature distribution across the combustion chamber and nozzle.

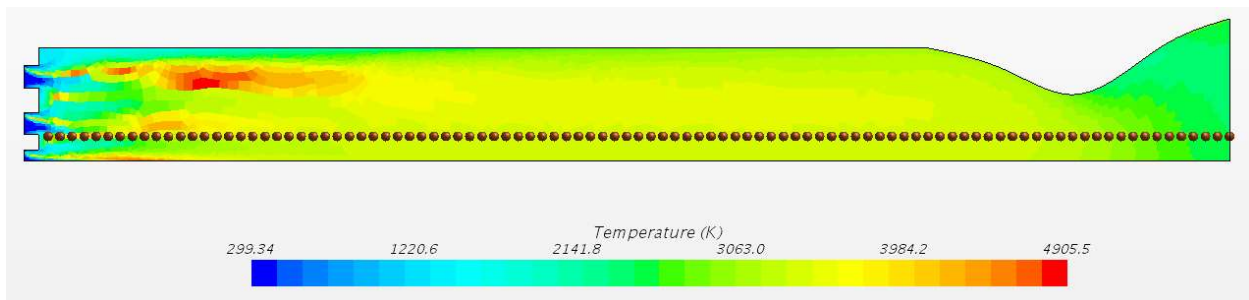


Figure 31. Qualitative temperature distribution across the chamber and nozzle.

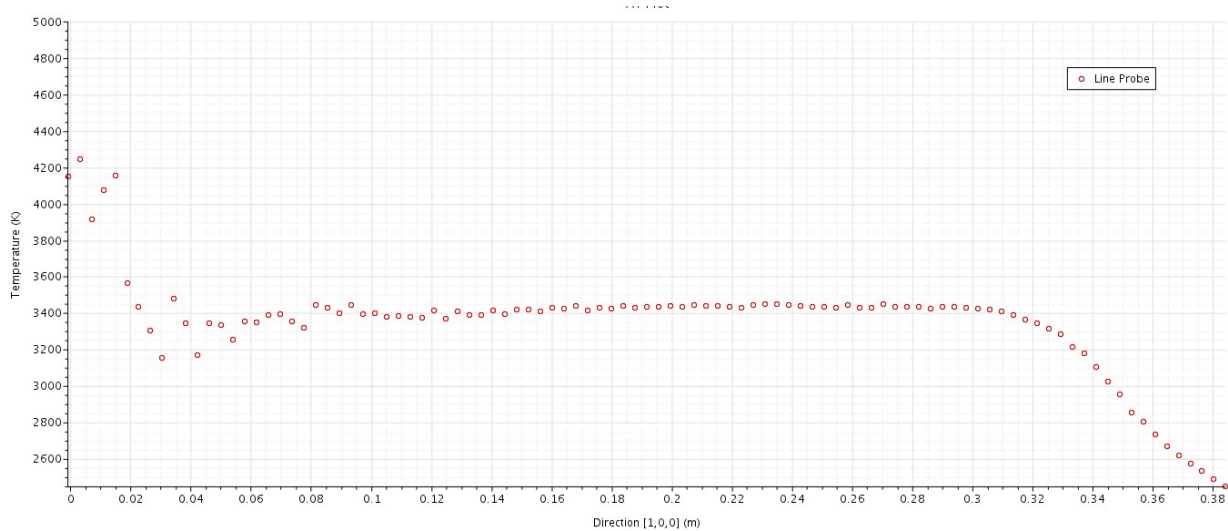


Figure 32. Quantitative temperature distribution across the chamber and nozzle.

Both figures show that the temperature increases from near 100 K to a steady 3400 K and then drops as the hot gaseous mixture is expanded through the supersonic nozzle. The temperature stabilizes at around a 100 mm into the combustion chamber and begins to drop at around the 320 mm mark. The initial spike in temperature is a result of the turbulent conditions in the initial combustion chamber area near the injectors. Comparing the temperature distribution graph between scenario 3 and scenarios 1 and 2, it can be seen that increasing hydrogen mass flow rate has decreased the overall achieved combustion chamber temperature drastically.

Figures 33 and 34 show the qualitative and quantitative pressure distribution across the combustion chamber and nozzle.

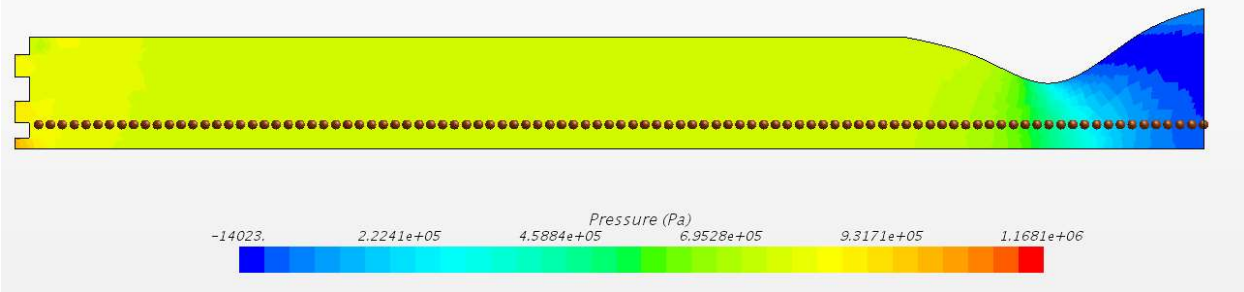


Figure 33. Qualitative pressure distribution across the chamber and nozzle.

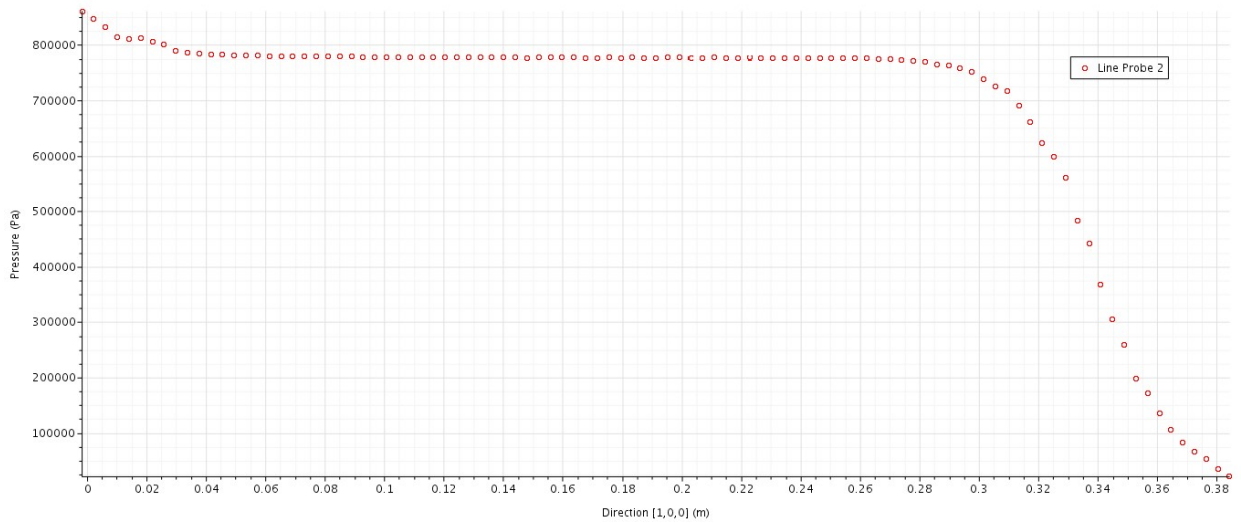


Figure 34. Quantitative pressure distribution across the chamber and nozzle.

Both figures show that the pressure stabilizes quickly to around 790 KPa after which it decreases drastically as the gaseous mixture is expanded through the supersonic nozzle. Comparing the pressure graphs between scenario 3 and scenarios 1 and 2, it can be seen that increasing the hydrogen mass flow rate has drastically increased the overall pressure within the combustion chamber.

## 10.6 Scenario 4: Higher Oxygen Mass Flow Rate

In this scenario the oxygen mass flow rate was increased to 8.0 kg/s while the kerosene and hydrogen mass flow rate were both set to 0.6325 kg/s.

### 10.6.1 Mole Concentration of Reactants and Products

Figure 35 shows the new variation in the concentration of oxygen.

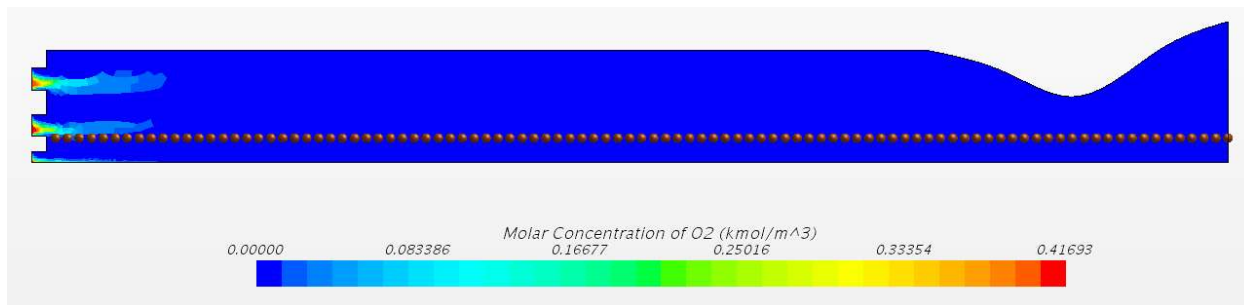


Figure 35. Oxygen concentration variation across the chamber and nozzle.

Figures 36 and 37 show the variation in the concentrations of the products of combustion: water and carbon-dioxide.

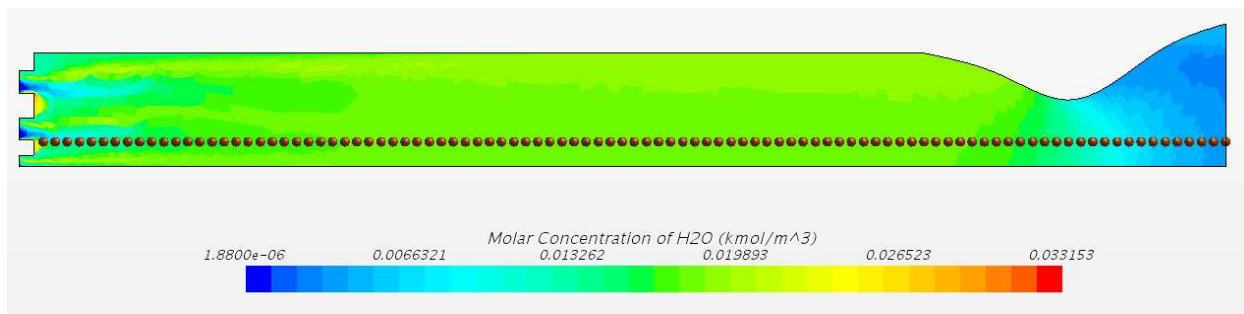


Figure 36. Water concentration variation across the chamber and nozzle.

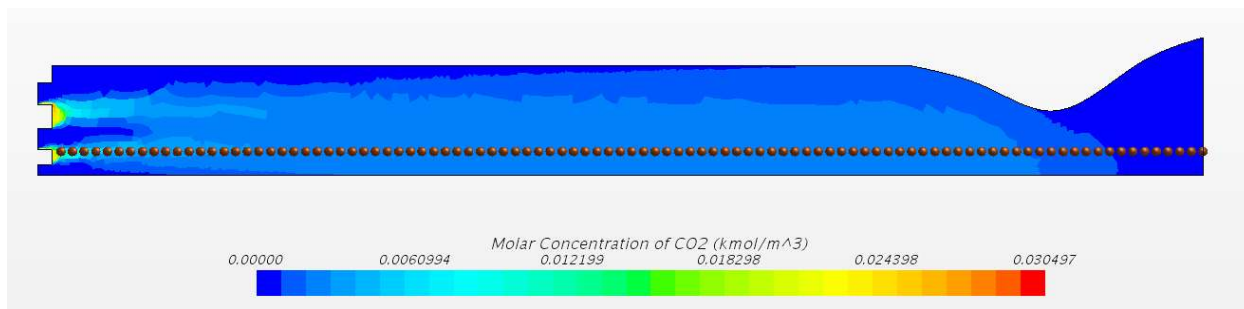


Figure 37. Carbon-dioxide concentration variation across the chamber and nozzle.

As can be seen from Figure 35 the concentration of oxygen is marginally higher near the injector region and the presence of oxygen lasts longer into the combustion chamber. The concentrations of kerosene and hydrogen do not change as much as they have the same mass flow rate as before. Figures 36 and 37 show that the full combustion of hydrogen, oxygen, and

kerosene still occurs by the end of the first third of the combustion chamber after which the concentration of water and carbon-dioxide dominates the mixture. Comparing the concentrations of water and carbon-dioxide between scenario 4 and scenarios 1, 2, and 3 there is a slight increase in the initial concentrations of water and carbon-dioxide in scenario 4 due to the increased mass flow rate of oxygen.

### 10.6.2 Temperature and Pressure Distribution

Figures 38 and 39 show the qualitative and quantitative temperature distribution across the combustion chamber and nozzle.

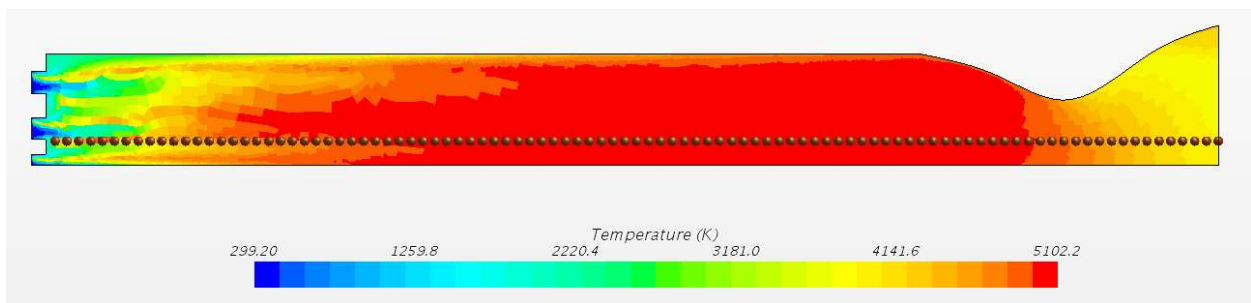


Figure 38. Qualitative temperature distribution across the chamber and nozzle.

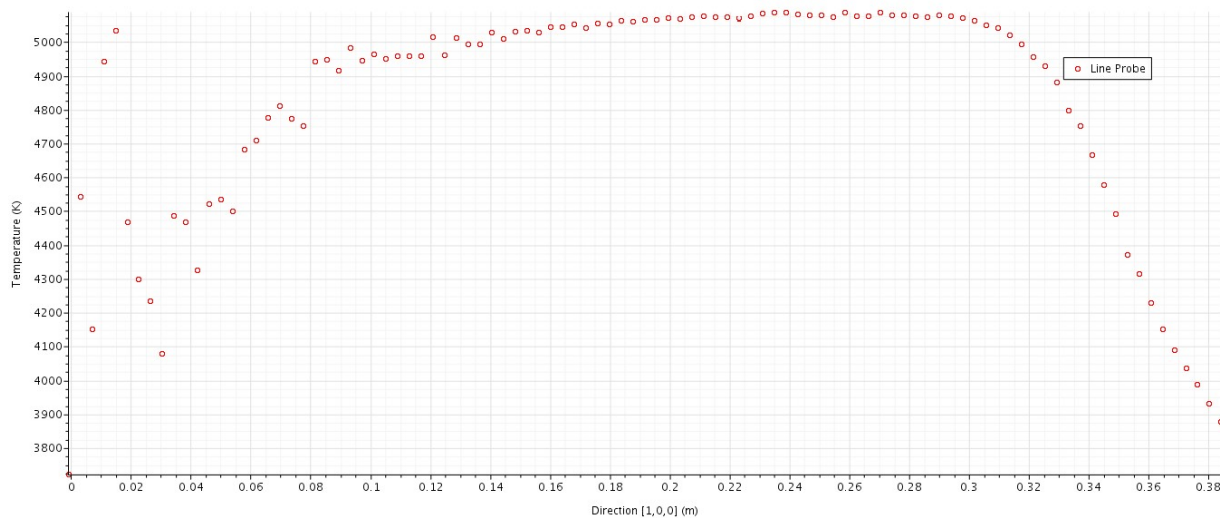


Figure 39. Quantitative temperature distribution across the chamber and nozzle.

Both figures show that the temperature increases from near 100 K to a steady 5050 K and then drops as the hot gaseous mixture is expanded through the supersonic nozzle. The temperature stabilizes at around a 160 mm into the combustion chamber and begins to drop at around the 320 mm mark. Comparing the temperature distribution graph between scenario 4 and scenarios 1, 2, and 3, it can be seen that increasing oxygen mass flow rate has greatly increased the overall achieved combustion chamber temperature.

Figures 40 and 41 show the qualitative and quantitative pressure distribution across the combustion chamber and nozzle.

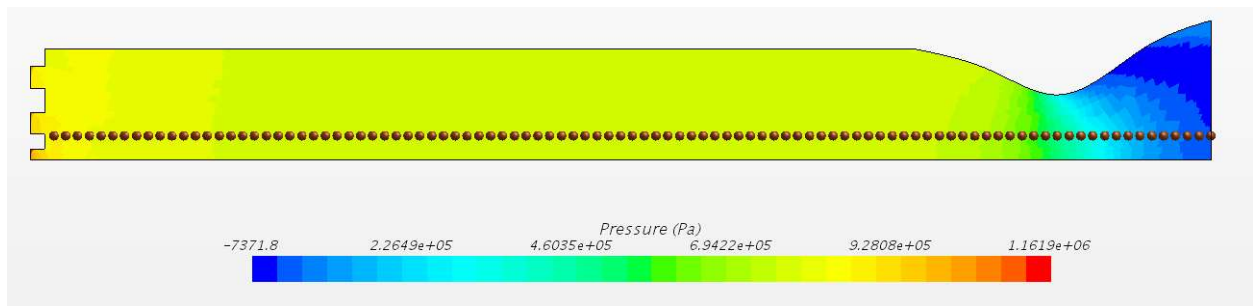


Figure 40. Qualitative pressure distribution across the chamber and nozzle.

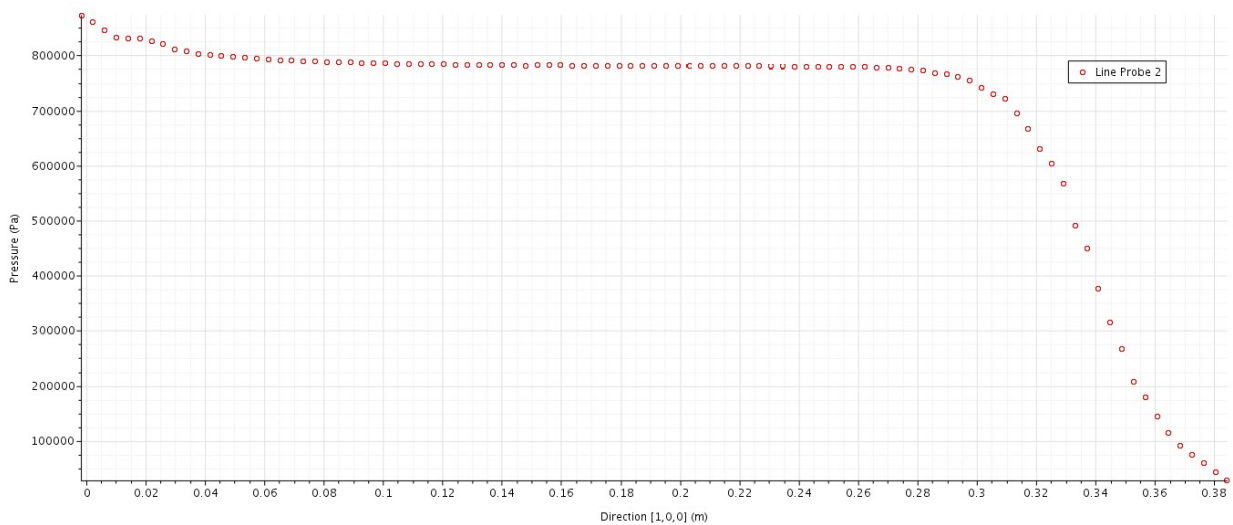


Figure 41. Quantitative pressure distribution across the chamber and nozzle.

Both figures show that the pressure stabilizes quickly to around 790 KPa after which it decreases drastically as the gaseous mixture is expanded through the supersonic nozzle. Comparing the pressure graphs between scenario 4 and scenarios 1, 2, and 3 it can be seen that increasing the oxygen mass flow rate has drastically increased the overall pressure within the combustion chamber when compared to scenarios 1 and 2 and is the same as in scenario 3.

## **10.7 Conclusion**

The primary purpose of this study was to use CFD to investigate tripropellant combustion systems. After a validation CFD simulation, based on a sub-scale hydrogen-oxygen combustion chamber, was done, four different scenarios for tripropellant combustion were studied. The first scenario looked at equal flow rates of hydrogen and kerosene and found that the combustion chamber temperature increased as compared to the hydrogen only case. The second scenario doubled the kerosene flow rate and found that the combustion chamber temperature was lower when compared to the first scenario. The third scenario doubled the hydrogen flow rate and found that the combustion chamber temperature was far lower than either two previous scenarios. Finally, the fourth scenario increased the flow rate of oxygen and resulted in higher chamber temperatures. Together the four scenarios showcase the complexity and trade-offs of varying different aspects of a tripropellant rocket engine. However, this study was only a small step in the use of CFD to study tripropellant combustion. Building on this study, future studies can look at the numerous other combinations of mass flow rates of hydrogen, kerosene, oxygen or even other fuels. Other aspects to investigate are different injection configurations for tripropellant systems.

## 9. References

- Anderson, J. D. (2019). Hypersonic and high-temperature gas dynamics. Reston, VA: American Institute of Aeronautics and Astronautics.
- Cai, H., Nie, W., Yang, X., Wu, R., & Su, L. (2017). Three-Dimensional Numerical Analysis of LOX/Kerosene Engine Exhaust Plume Flow Field Characteristics. *International Journal of Aerospace Engineering*, 2017, 1-13. doi:10.1155/2017/4768376
- Cheng, G., & Farmer, R. (2002). CFD spray combustion model for liquid rocket engine injector analyses. *40th AIAA Aerospace Sciences Meeting & Exhibit*. doi:10.2514/6.2002-785
- Farmer, Richard C., Cheng, Gary C., Anderson, Peter G. (1997). Development of Tripropellant CFD Design Code.
- Garg, P., Sharma, A., Agarwal, D. K., & Varma, M. (2017). Numerical Modeling of Liquid Oxygen and Kerosene Combustion at High Pressures. *55<sup>th</sup> AIAA Aerospace Sciences Meeting*. doi:10.2514/6.2017-2023
- Gontcharov, N. S., Orlov, V. A., Rachuk, V. S., Rudis, M. A., Starke, R. G., & Hulka, J. R. (2004). Tripropellant Engine Technology for Reusable Launch Vehicles. *Liquid Rocket Thrust Chambers*, 649-682. doi:10.2514/5.9781600866760.0649.0682
- Khan, M. F., Quadri, Z. A., Kulkarni, P. S., Guven, U., Bhat, S. P., & Sundarraj, K. (2013). CFD Simulation of a Liquid Rocket Propellant (LH2/LOx) Combustion Chamber. *15th Annual CFD Symposium*. Retrieved February 24, 2019.
- Kmiec, T. D., & Carroll, R. G. (n.d.). Tripropellant Combustion Process. *United Technologies Corporation, Pratt and Whitney*, 316-333. Retrieved February 26, 2019.
- Prelik, D., Wiedmann, D., Oechslein, W., & Kretschmer, J. (1998). *Cryogenic rocket calorimeter chamber experiments and heat transfer simulations*. 34th AIAA/ASME/SAE/ASEE Joint Propulsion Conference and Exhibit. doi:10.2514/6.1998-3440
- STAR-CCM. (n.d.). Retrieved from <https://mdx.plm.automation.siemens.com/star-ccm-plus>
- Sutton, G. P., & Biblarz, O. (2017). Rocket propulsion elements. Hoboken (N.Y.): Wiley.
- Vongpaseuth, T., Venkatasubramanyam, G., & Martin, J. (1995). Russian tripropellant engines for SSTO. *31<sup>st</sup> Joint Propulsion Conference and Exhibit*. doi:10.2514/6.1995-2952
- Wang, T., & Chen, Y. (1993). Unified Navier-Stokes flowfield and performance analysis of liquid rocket engines. *Journal of Propulsion and Power*, 9(5), 678-685. doi:10.2514/3.23675
- Zhukov, Victor P. (2015). Modelling of Combustion and Heat Transfer in Rocket Combustion Chambers Using CFX.